

# The MACHO Project LMC Microlensing Results from the First Two Years and the Nature of the Galactic Dark Halo

C. Alcock<sup>1,2</sup>, R.A. Allsman<sup>3</sup>, D. Alves<sup>1,4</sup>, T.S. Axelrod<sup>5</sup>, A.C. Becker<sup>2,6</sup>, D.P. Bennett<sup>1,2,4,7</sup>,  
 K.H. Cook<sup>1,2</sup>, K.C. Freeman<sup>5</sup>, K. Griest<sup>2,8</sup>, J. Guern<sup>2,8</sup>, M.J. Lehner<sup>2,8</sup>, S.L. Marshall<sup>1,2</sup>,  
 B.A. Peterson<sup>5</sup>, M.R. Pratt<sup>2,6,9</sup>, P.J. Quinn<sup>10</sup>, A.W. Rodgers<sup>5</sup>, C.W. Stubbs<sup>2,6</sup>, W. Sutherland<sup>11</sup>,  
 D.L. Welch<sup>12</sup>

(The MACHO Collaboration)

Submitted to ApJ, 24 June 1996

## ABSTRACT

The MACHO Project is a search for dark matter in the form of massive compact halo objects (Machos). Photometric monitoring of millions of stars in the Large Magellanic Cloud (LMC), Small Magellanic Cloud (SMC), and Galactic bulge is used to search for gravitational microlensing events caused by these otherwise invisible objects. Analysis of the first 2.1 years of photometry of 8.5 million stars in the LMC reveals 8 candidate microlensing events. This is substantially more than the number expected ( $\sim 1.1$ ) from lensing by known stellar populations. The timescales ( $\hat{t}$ ) of the events range from 34 to 145 days. We estimate the total microlensing optical depth towards the LMC from events with  $2 < \hat{t} < 200$  days to be  $\tau_2^{200} = 2.9_{-0.9}^{+1.4} \times 10^{-7}$  based upon our 8 event sample. This exceeds the optical depth,  $\tau_{\text{backgnd}} = 0.5 \times 10^{-7}$ , expected from known stars, and the difference is to be compared with the optical depth predicted for a “standard” halo composed entirely of Machos:  $\tau_{\text{halo}} = 4.7 \times 10^{-7}$ . To compare with Galactic halo models, we perform likelihood analyses on the full 8 event sample and a 6 event subsample (which allows for 2 events to be caused by a non-halo “background”). This gives a fairly model independent estimate of the halo mass in Machos within 50 kpc of  $2.0_{-0.7}^{+1.2} \times 10^{11} M_{\odot}$ , which is about half of the “standard halo” value. We also find a most probable Macho mass of  $0.5_{-0.2}^{+0.3} M_{\odot}$ , although this value is strongly model dependent. Additionally, the absence of short duration events places stringent upper limits on the contribution of low-mass Machos: objects from  $10^{-4} M_{\odot}$  to  $0.03 M_{\odot}$  contribute  $\lesssim 20\%$  of the “standard” dark halo.

*Subject headings:* dark matter - gravitational lensing - Stars: low-mass, brown dwarfs, white dwarfs

---

<sup>1</sup>Lawrence Livermore National Laboratory, Livermore, CA 94550

Email: `alcock`, `alves`, `bennett`, `kcook`, `stuart@igpp.llnl.gov`

<sup>2</sup>Center for Particle Astrophysics, University of California, Berkeley, CA 94720

<sup>3</sup>Supercomputing Facility, Australian National University, Canberra, ACT 0200, Australia

Email: `robyn@macho.anu.edu.au`

<sup>4</sup>Department of Physics, University of California, Davis, CA 95616

<sup>5</sup>Mt. Stromlo and Siding Spring Observatories, Australian National University, Weston, ACT 2611, Australia

Email: `tsa`, `kcf`, `peterson`, `alex@mso.anu.edu.au`

<sup>6</sup>Departments of Astronomy and Physics, University of Washington, Seattle, WA 98195

Email: `becker`, `mrp`, `stubbs@astro.washington.edu`

<sup>7</sup>Department of Physics, University of Notre Dame, Notre Dame, IN 46556

<sup>8</sup>Department of Physics, University of California, San Diego, La Jolla, CA 92093

Email: `kgriest`, `jguern`, `mlehner@ucsd.edu`

<sup>9</sup>Department of Physics, University of California, Santa Barbara, CA 93106

<sup>10</sup>European Southern Observatory, Karl-Schwarzschild Str. 2, D-85748, Garching, Germany

Email: `pjq@eso.org`

<sup>11</sup>Department of Physics, University of Oxford, Oxford OX1 3RH, U.K. Email: `w.sutherland@physics.ox.ac.uk`

<sup>12</sup>Dept. of Physics & Astronomy, McMaster University, Hamilton, Ontario, Canada L8S 4M1. Email: `welch@physics.mcmaster.ca`

## 1. Introduction

Following the suggestion of Paczyński (1986), many groups are now engaged in searches for dark matter in the form of massive compact halo objects (Machos) using gravitational microlensing, and many candidate microlensing events have been reported. Detailed reviews of microlensing are given by Roulet & Mollerach (1996) and Paczyński (1996).

The expected microlensing rate towards the Magellanic Clouds due to a Macho-dominated halo comfortably exceeds the expected microlensing rate from known populations of low-mass stars. Thus, our LMC survey directly probes the Macho content of the halo. We have previously reported 4 microlensing candidates towards the LMC (Alcock *et al.* 1993, 1994, 1995a, 1996a, hereafter A96); the EROS group has reported 2 candidates (Aubourg *et al.* 1993), but 1 of these is an eclipsing binary star (Ansari *et al.* 1995) and hence is suspect. These events have characteristic timescales  $\hat{t} \sim 20 - 60$  days; searches for short-timescale events with  $1 \text{ hour} \lesssim \hat{t} \lesssim 10$  days have revealed no candidates to date (Aubourg *et al.* 1995; Alcock *et al.* 1996d) and set interesting limits on low-mass Machos.

The results from the two groups are consistent after accounting for the different sample sizes and detection efficiencies; a robust result is that substellar Machos from  $10^{-6}$  to  $10^{-2} M_{\odot}$  cannot make up the entire ‘standard’ halo mass of  $4.1 \times 10^{11} M_{\odot}$  within 50 kpc.

However, it is very interesting that the number of previously detected LMC events appears significantly higher than expected from lensing by known stellar populations; thus, there were a range of plausible explanations outlined by A96. These included a halo containing  $\sim 20\%$  Machos, a ‘minimal’ all-Macho halo, Machos in a thick disk or spheroid, a statistical fluctuation in the stellar lensing rate, or variable stars masquerading as microlensing events.

A larger sample can help to distinguish between these alternatives. In this paper we present analysis of our first 2.1 years of observations of 8.5 million stars in the LMC; this dataset comprises the same set of stars analyzed in Alcock *et al.* (1995a) and A96, but with twice the timespan and improved selection criteria.

The role of the unexpectedly large number of events (currently  $> 100$ ) seen in the direction of the Galactic bulge (Udalski *et al.* 1994a; Alcock *et al.*

1995b; Alcock *et al.* 1996b; Alard *et al.* 1995a) is indirect. While these results are very interesting as a verification of microlensing, as a probe of Galactic structure and the mass functions of the disk and bulge, and as a possible avenue for detection of planets (Mao & Paczyński 1991; Gould & Loeb 1992; Bennett & Rhie 1996; Tytler 1995), bulge microlensing does not directly probe halo dark matter. Our experience with bulge microlensing has taught us much, however, and has helped us to refine our event selection criteria.

The plan of the paper is as follows: in § 2 we outline the observations and photometric reductions, and in § 3 we describe microlensing event selection, and the resulting candidates; in § 4 we estimate our detection efficiency. In § 5 we show the distributions of the selected events in the color-magnitude diagram, on the sky, and according to impact parameter. In § 6 we provide various analyses of the sample, using both the total number of events and the individual timescales. We discuss our conclusions in § 7.

Note that many of the reduction and analysis procedures used here are very similar to those in A96, to which we refer extensively. The reader is encouraged to consult that paper to understand the details of the experiment, but we repeat the main points here for clarity.

## 2. Observations and Photometric Reductions

The MACHO Project has had full-time use of the 1.27-meter telescope at Mount Stromlo Observatory, Australia, since 1992 July; an extended run until 1999 December has recently been approved. Details of the telescope system are given by Hart *et al.* (1996) and of the camera system by Stubbs *et al.* (1993) and Marshall *et al.* (1994). Briefly, corrective optics and a dichroic are used to give simultaneous imaging of a  $42 \times 42$  arcmin<sup>2</sup> field in two colors, using eight 2048<sup>2</sup> pixel CCDs.

As of 1996 June, over 44000 exposures have been taken with the system, over 3 TBytes of raw image data. About 60% are of the LMC, the rest are of fields in the Galactic center and SMC.

In this paper, we consider the first 2.1 years of data from 22 well-sampled fields, located in the central  $\sim 5^{\circ} \times 3^{\circ}$  of the LMC; field centers are listed in Table 1, and shown in Figure 1.

The observations described here comprise 10827 images distributed over the 22 fields. These include

Fig. 1.— An R-band image of the LMC, 8.2 degrees on a side (G. Bothun, private communication), showing the locations of the 22 MACHO fields used here.

virtually all of our observations of these fields in the time span of 769 days from 1992 September 18 to 1994 October 26 as well as a fraction of our observations taken between 1992 July 22 and 1992 August 23 when our system was still in an engineering phase. We obtained at least one observation on 556 of the 769 nights. The mean number of exposures per field is  $10827/22 = 492$ , with a range from 300 to 785. The sampling varies between fields (Table 1), since the higher priority fields were often observed twice per night with a  $\sim 4$  hour spacing. There was a 50-day gap in observations after 1993 November 29, following a fire in an electronics box in the control room. The telescope and CCD cameras were not affected, so there is no systematic difference in the data before and after the fire.

The photometric reduction procedure was very similar to that described in A96; briefly, a good-quality image of each field is chosen as a template, and used to generate a list of stellar positions and magnitudes. All other images are aligned with the template using fiducial stars, and a PSF is measured from these. Then, the flux of all other stars is fitted using the known positions and PSF. For each measurement we also compute an error estimate and six quality flags; these flags are the object type, the  $\chi^2$  of the PSF fit, a crowding parameter, a local sky estimate, and the fraction of the star’s flux rejected due to bad pixels and cosmic rays. The resulting data are reorganized into stellar lightcurves, and searched for variable stars and microlensing events.

There is a minor complication to which we will refer later. For software-related reasons, we used different templates for the first and second year’s reductions of 6 of our fields. Thus there is not a one-to-one correspondence between the set of stars in the 2 distinct years, and the 2 years had to be analyzed separately. We chose to make this split between the pre-fire and post-fire data to minimize the chance of an event spanning the 2 data sets.

### 3. Event Detection

The data set used here comprises some 9 billion individual photometric measurements. Discriminating genuine microlensing from stellar variability and systematic photometry errors is not an easy task. The significance of the results we report in this paper is critically dependent upon the event selection criteria we employ.

The determination of our event selection criteria could not be made before looking in detail at the lightcurves. The selection criteria should accept ‘true’ microlensing events, and reject events due to intrinsic stellar variability and instrumental effects. The MACHO Project is the largest survey of astronomical variability in history, which means that we had to learn how to perform event selection from the data we gather; it was not possible to develop meaningful selection criteria independent of the data.

The first step in the event selection process is to use the photometry quality flags (defined above) to reject suspect data points, and to require a combination of good time coverage and high significance such that systematic photometry errors do not produce false detections. These steps leave us with lightcurves in which we can expect to separate microlensing events from intrinsic stellar variability. We exploit the features of microlensing that distinguish it from intrinsic stellar variability, and also to explicitly exclude from our sample stars that reside in regions of the color-magnitude diagram that are prone to variability.

We compute for each light curve a set of temporal variability statistics, and we have developed a set of criteria (“cuts”) that we use to distinguish microlensing from the noise. These criteria have evolved over the course of the experiment. The cuts used to detect the 3 LMC events reported in Alcock *et al.* (1995a) and A96 were derived from Monte Carlo simulations of microlensing events added to our early data. We have refined these cuts for the analysis reported here.

In this regard, our experience with the Galactic bulge has been especially helpful. Since our previous analysis of a smaller set of LMC data (Alcock *et al.* 1995a, A96), we have analyzed a large set of data towards the Galactic bulge (Alcock *et al.* 1996b; Pratt *et al.* 1995), which has yielded over 80 microlensing events. These observations provide a more realistic set of microlensing events than the artificial events we have used previously to test our analysis procedures.

Of the 43 bulge events from the 1993 bulge season (Alcock *et al.* 1996b), 14 would have failed the cuts used in our previous LMC analysis. A number of these events fail the cuts described in A96 because they are not well described by the “normal” microlensing light curve which assumes a single point lens, constant velocities, and an unblended source star. Using the nomenclature of Alcock *et al.* (1996b), events 119-A and 104-C have large deviations from the “normal” microlensing lightcurves due to a binary lens (for 119-

A) and the orbital motion of the Earth (for 104-C). Event lightcurves can also deviate from “normal” if the lensed star’s image is blended with another star which is within the same seeing disk but is not lensed. The lightcurves of events 115-A, 128-A, 159-B, and 162-B appear to indicate significant blending which causes them to fail the LMC year-1 cuts on the fit  $\chi_{ml}^2$ , the fit  $\chi_{ml}^2$  in the peak region, and/or the event chromaticity. Two other 1993 bulge events also fail the fit  $\chi_{ml}^2$  or fit “peak”  $\chi_{ml}^2$  cuts. These are event 119-B which appears to have a couple of photometric outliers which barely pass our photometric quality cuts, and event 128-B which has excess scatter in the unmagnified portion of the lightcurve for reasons that are not yet understood. We also find that events 101-D, 111-A, 111-B, 124-A, and 159-A fail our cuts on lightcurve coverage while event 104-B fails our LMC year-1 crowding cut.

Many of these bulge events which fail the LMC year-1 cuts, such as events 101-D, 119-B, 128-A and 159-B as well as the exotic microlensing events 104-C and 119-A appear by eye to be very high quality microlensing events. In contrast, LMC events 2 and 3 of (Alcock *et al.* 1995a) which passed the year-1 cuts appear far less striking. Our data clearly indicate that these stars have brightened, but the signal-to-noise for these events is too low to say much about the shape of their lightcurves. Thus, we are more confident that these bulge events are actual microlensing events than we are that LMC events 2 and 3 were caused by microlensing. This has motivated us to modify our selection criteria for this combined year 1 and 2 data. As described below, we have modified our cuts so as to allow more “high quality” events similar to the events seen towards the bulge.

Note that as long as the experiment’s event *detection efficiency* is calculated properly, and the *selection criteria* are sufficiently stringent to accept only real microlensing events, changes in the selection criteria will be accounted for in the efficiency calculations, and the details will not affect the final results, *i.e.* the microlensing optical depth, the halo mass, and macho mass estimates.

We have made the following changes to the selection criteria. We have loosened a cut on stellar crowding which removed stars which are severely blended with their neighbors under typical seeing conditions, and we have loosened our cuts on the stellar object type defined by our photometry code. We loosened a cut on the average photometric error, allowing sensi-

tivity to high magnification events on very faint stars. We have also dropped our previous cut on event chromaticity. Although theoretical microlensing events must be achromatic, our target stars are often blended with stars of different colors, so observed microlensing events can appear to have some color dependence. (There is a generalization of the chromaticity test that allows for blending. It is used below to check each selected event, but we do not use this procedure for event selection.)

As a result of these changes, we have found it necessary to increase some of our signal-to-noise cuts to compensate for the increased background that the above changes allow. This reduces the chances of detecting low signal-to-noise lensing events.

Another change in our analysis procedure was motivated by the fact that  $\sim 5\%$  of the microlensing events seen toward the bulge show significant deviations from the normal point source, point lens, constant velocity microlensing light curve. These effects include binary lenses (Udalski *et al.* 1994b; Bennett *et al.* 1995a; Pratt *et al.* 1995; Alard *et al.* 1995b), an event showing asymmetry due to the orbit of the Earth (Alcock *et al.* 1995c), and an event showing the effect of the finite source size (Alcock *et al.* 1996g). These are often quite spectacular examples of gravitational microlensing events, but they are poorly fit by a normal microlensing light curve. As a result, cuts on the  $\chi_{ml}^2$  of the normal microlensing event fit can preferentially remove these exotic events resulting in a microlensing detection efficiency that is lower than predicted based upon a set consisting of “normal” events. In the present analysis, we have taken some steps to reduce our dependence on  $\chi_{ml}^2$  in the region of lensing magnification, and this has paid off with the discovery of a binary microlensing event, but our efficiency for detecting exotic microlensing events is probably still somewhat lower than for “normal” lensing events.

We have summarized the old and new selection criteria in Table 2; these are described in more detail below.

### 3.1. Selection Criteria

Before starting the microlensing search, measurements with questionable PSF chi squared, crowding, missing pixel, or cosmic ray flags are flagged as suspect measurements and removed from further consideration. We require that stars have an acceptable

template measurement, and at least 7 simultaneous red-blue data pairs, to be searched for microlensing. The reddest  $\approx 0.5\%$  of stars, those with  $V - R > 0.9$ , are excluded from the microlensing search because they are usually long-period variables. The event detection then proceeds in two stages. The first stage, to define a loose collection of candidate events, is very similar to that described in A96; a set of matched filters of timescales 7, 15 and 45 days is run over each lightcurve. If after convolution, a lightcurve shows a peak above a pre-defined significance level in both colors, it is defined as a ‘level-1 candidate’, a full 5-parameter fit to microlensing is made, and many statistics describing the significance of the deviation, goodness of fit, etc. are calculated. We use the standard point-source, point-lens approximation, in which the magnification  $A$  is given by (Refsdal 1964)

$$\begin{aligned} A(u) &= \frac{u^2+2}{u\sqrt{u^2+4}} \\ u &= b/r_E \\ r_E &= \sqrt{\frac{4Gml(L-l)}{c^2 L}} \end{aligned} \quad (1)$$

where  $b$  is the separation of the lens from the undeflected line of sight,  $r_E$  is the Einstein radius (in the lens plane),  $l$ ,  $L$  are the distances to the lens and source, and  $m$  is the lens mass. Assuming also uniform motion, the fit to microlensing takes the form

$$\begin{aligned} f_R(t) &= A(t)f_{0R}, & f_B(t) &= A(t)f_{0B} \\ A(t) &= A(u(t)) \\ u(t) &= \left[ u_{\min}^2 + \left( \frac{2(t-t_{\max})}{\hat{t}} \right)^2 \right]^{0.5} \end{aligned} \quad (2)$$

where the 5 free parameters are the baseline flux in red and blue passbands  $f_{0R}$ ,  $f_{0B}$ , and the 3 parameters of the microlensing event: the minimum impact parameter in units of the Einstein radius  $u_{\min}$ , the Einstein diameter crossing time  $\hat{t} \equiv 2r_E/v_{\perp}$ , and the time of maximum magnification  $t_{\max}$ . Later, we will often quote the more observable fit maximum magnification  $A_{\max} \equiv A(u_{\min})$  instead of  $u_{\min}$ .

Lightcurves passing loose cuts on these statistics are defined as ‘level-1.5’ candidates, and are output as individual files along with their associated statistics. In the present analysis, there were approximately 390,000 level-1 candidates, of which about 29,000 passed the level-1.5 criteria. More stringent cuts are then applied to select final ‘level-2’ candidates.

As explained above, the criteria for ‘final’ microlensing candidates have been modified from those used in A96. An important parameter that is used for a number of the cuts is  $\Delta\chi^2 \equiv \chi_{\text{const}}^2 - \chi_{ml}^2$  where  $\chi_{\text{const}}^2$  and  $\chi_{ml}^2$  are the  $\chi^2$  values for the constant flux and (unblended) microlensing fits respectively;  $\Delta\chi^2$  is the effective ‘significance’ of the event summed over all data points.  $\chi_{\text{peak}}^2$  refers to the  $\chi^2$  of the microlensing fit in the ‘‘peak’’ region where  $A_{\text{fit}} > 1.1$ .  $N_{\text{dof}}$  refers to the number of degrees of freedom in a particular fit. We use the following criteria to select candidate microlensing events:

- 1) The fitted time of peak magnification  $t_{\max}$  must be within the time span of the observations, and the event duration  $\hat{t} < 300$  days.
- 2) We require that the star should show a roughly constant baseline: there must be at least 40 ‘baseline’ points outside the time interval  $t_{\max} \pm 2\hat{t}$ , and the reduced  $\chi^2$  of the microlensing fit outside this interval must be  $\chi_{ml-out}^2/N_{\text{dof}} < 4$ .
- 3) We require that  $A_{\max} > 2 \times$  the mean estimated error of the data points.
- 4) We require at least 6 data points  $> 1\sigma$  above median brightness in the peak region  $t_{\max} \pm 0.5\hat{t}$ . This excludes candidate events which may be caused by one or two discrepant observations, most commonly un-flagged cosmic rays, satellite tracks, poor telescope tracking etc.
- 5) We exclude stars brighter than  $V < 17.5$  which contain a class of bright blue variables known as ‘‘bumpers’’ (Alcock *et al.* 1996f).
- 6) We exclude stars in a  $10' \times 10'$  region surrounding SN 1987A in order to avoid spurious microlensing triggers due to the supernova light echo.
- 7) We remove events with low signal to noise or a poor peak fit by requiring  $\Delta\chi^2/(\chi_{\text{peak}}^2/N_{\text{dof}}) > 200$ .
- 8) We remove stars that may have crowding related spurious photometry; those stars for which over 5% of the measurements have been rejected due to crowding.
- 9) We require a crowding dependent signal/noise criteria: crowding measure  $< 70 \log_{10}[\Delta\chi^2/(\chi_{ml}^2/N_{\text{dof}})] - 45$ . This cut requires extra signal-to-noise for

stars with very close neighbors and removes a class of spurious triggers caused by PSF anomalies due to transient problems with the telescope optics.

- 10) Our main signal-to-noise cut is  $\Delta\chi^2/(\chi_{ml}^2/N_{dof}) > 500$ .
- 11) We require a fit  $A_{\max} > 1.75$ .

These cuts are summarized in Figure 2, which illustrates cuts (10) and (11) for all events that pass cuts (1)-(4) and (6).

Events that pass all cuts except for (10) and (11) are indicated with circles, while the open symbols and crosses indicate events which failed 1 or more of cuts (5), (7)-(9). Open squares indicate events which fail cut (5), and open triangles indicate events which fail cut (7). The crosses indicate events which fail cuts (8) or (9). Note that while most of these events were discovered prior to the selection of the final set of cuts, the event closest to the cut boundaries was not discovered until this set of cuts was run. This is the binary lens event with a single lens fit  $A_{\max} = 1.86$ . The lightcurves passing all of these selection criteria are further investigated, as outlined below. The effect of the variation of these cuts on our results are discussed in Section 6.3 below.

### 3.2. Microlensing Candidates

Twelve lightcurves passed the cuts discussed above, indicated by the open and closed circles in the upper right hand region of Figure 2. The lightcurves are shown in Figure 3, their fit parameters are listed in Table 3, and finding charts for each star are shown in Figure 4. Parameters for fits including the possibility of blending with an unlensed star in the same seeing disk as the lensed star are given in Table 4. Four of these lightcurves (1a, 1b, 12a and 12b) actually correspond to two stars which occur in field overlap regions; the two lightcurves for each star are based on independent data and reductions.

We are very confident that these events are of astrophysical origin and not due to systematic photometry errors. First, they show very significant changes in brightness over each of many individual CCD images over many weeks. Due to pointing variations, a given star moves by many pixels between exposures, and may move to different chips when the telescope moves across the mounting pier; so the events cannot

be due to uncatalogued CCD defects. Two of these events are independently detected in field overlaps, event 1 has been confirmed in the EROS plate data (Aubourg *et al.* 1993), and event 4 was confirmed by E. Giraud at ESO (Giraud 1994).

Once again the experience with the Galactic bulge is helpful. A number of bulge events which have been observed from multiple sites. We re-discovered the events OGLE#1 and OGLE#7 in our data (Alcock *et al.* 1996b). OGLE rediscovered our Alert 95-11, Most of our  $\sim 40$  bulge “alert” events were observed at other sites (Alcock *et al.* 1996c; Pratt *et al.* 1995; Szymanski *et al.* 1994); so far, none has turned out to be due to observational error, even though the criteria for an alert event are less stringent than those used for this sample. These multi-site detections convince us that the events we describe are astrophysical in origin.

We now give a brief discussion of the individual events, with follow-up observations and a subjective quality classification.

Event 1 was our first discovery (Alcock *et al.* 1993), and has remained constant as expected in the following year. The star’s spectrum is that of a normal clump giant at the radial velocity of the LMC (Della Valle 1994). In view of the high signal to noise, achromaticity, and good fit to microlensing, we classify this as an excellent microlensing candidate.

The low signal-to-noise candidates 2 and 3 from Alcock *et al.* (1995a) and A96 *do not pass* the final cuts used for this data set; thus, they are not included in Table 3, but we have numbered the present set of 10 candidates 1, 4 . . . 12 to avoid possible ambiguity. As shown in Figure 2, event 2 fails cut (10) and event 3 fails cuts (10) and (11); this is due to the changes that have been made in our cuts as noted above. Although the star involved in event 2 appeared constant during the second year data, the EROS group has informed us that it may have brightened in 1990, and it has shown indication of further brightening episodes in our data in 1995 January & December; thus it is probably a variable star. The star involved in event 3 has not shown further variation, and may have been a microlensing event, but it does not pass our revised selection criteria.

Event 4 was the first LMC microlensing candidate detected in progress; it was detected by our real-time Alert system (Pratt *et al.* 1995) on 1994 October 8, and announced in IAU Circular 6095. This accounts



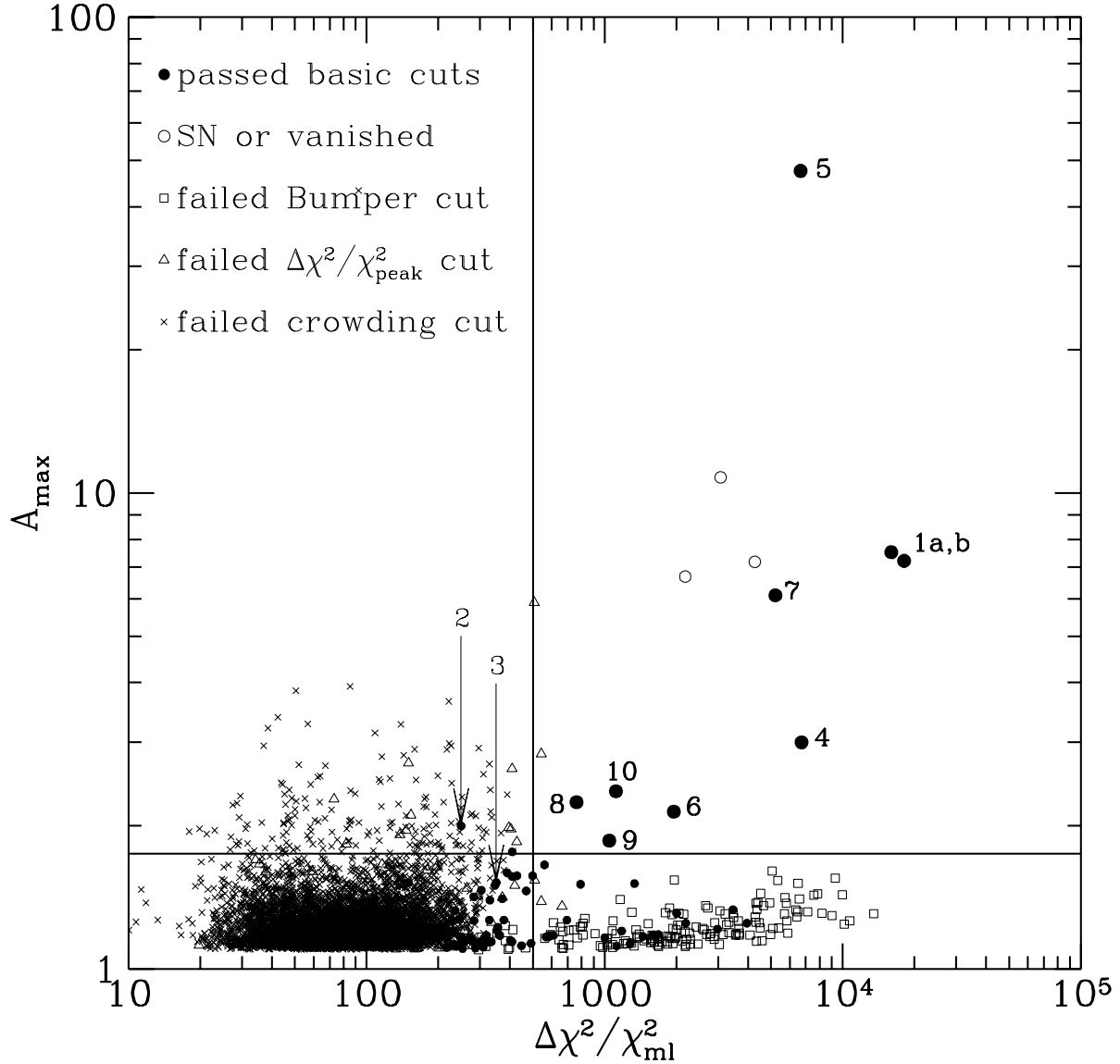


Fig. 2.— The final cuts for selection of microlensing candidates. The x-axis is  $\Delta\chi^2/\chi_{ml}^2$ , where  $\Delta\chi^2 \equiv \chi_{const}^2 - \chi_{ml}^2$  is the improvement in  $\chi^2$  between a constant brightness fit and a microlensing fit. The y-axis is the fitted maximum magnification. The symbols are explained in § 3.1. The solid lines show the final cuts (10) and (11); the circles in the upper right are the 12 events (10 stars) discussed in § 3.2. Events 2 and 3 from A96 are also indicated.

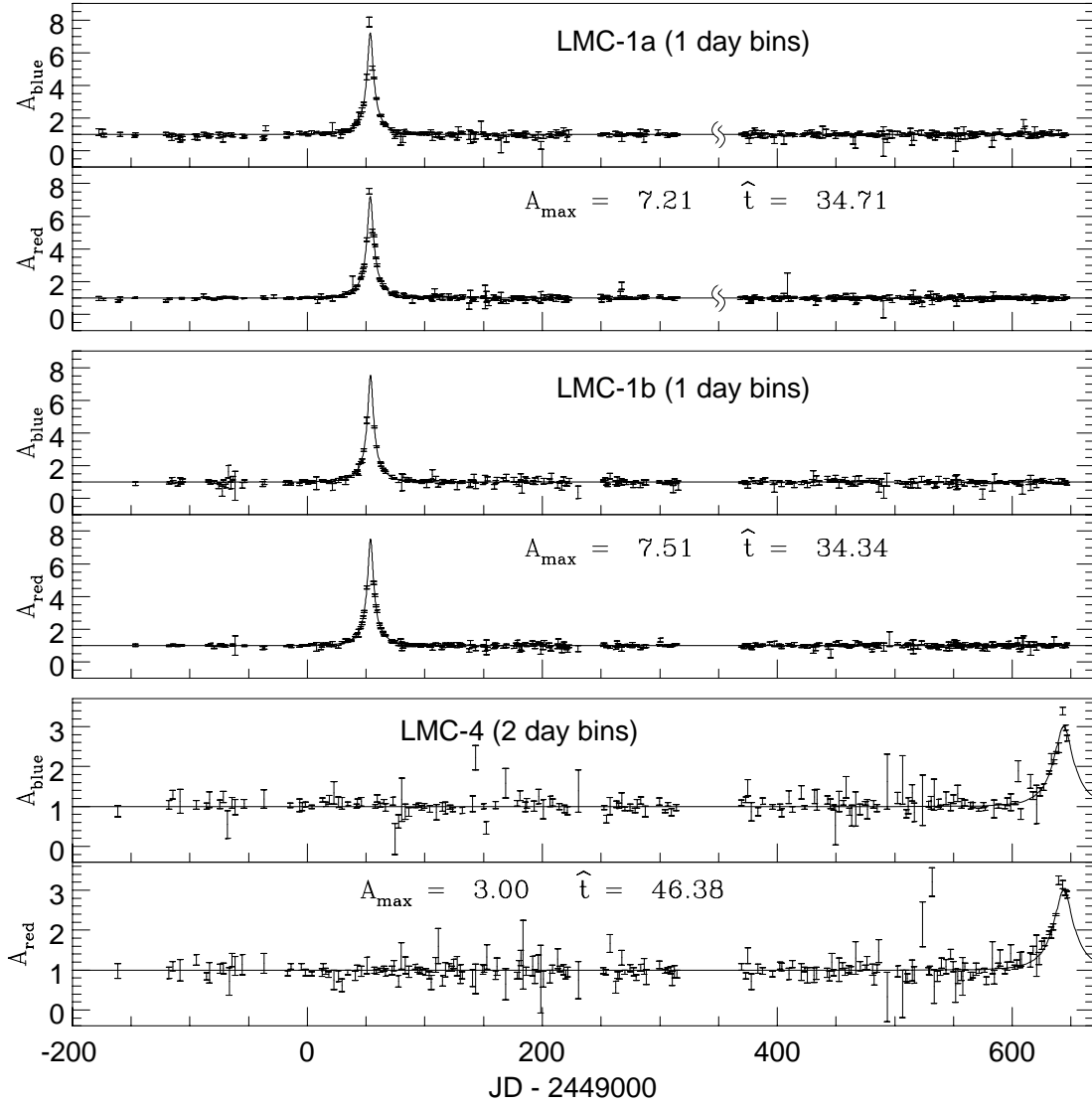


Fig. 3.— The lightcurves for the 12 candidates (10 stars) in § 3.2. For each object, the upper and lower panels show blue and red passbands. Flux is in linear units with  $1\sigma$  estimated errors, normalized to the fitted unlensed brightness. For clarity, the points shown are averages in time bins roughly matched to the event timescales, as indicated on each panel. For events 1a, 6 and 8, the wavy lines indicate that different templates were used before and after day 330; thus a separate baseline normalization has been used for each portion; see § 2 .

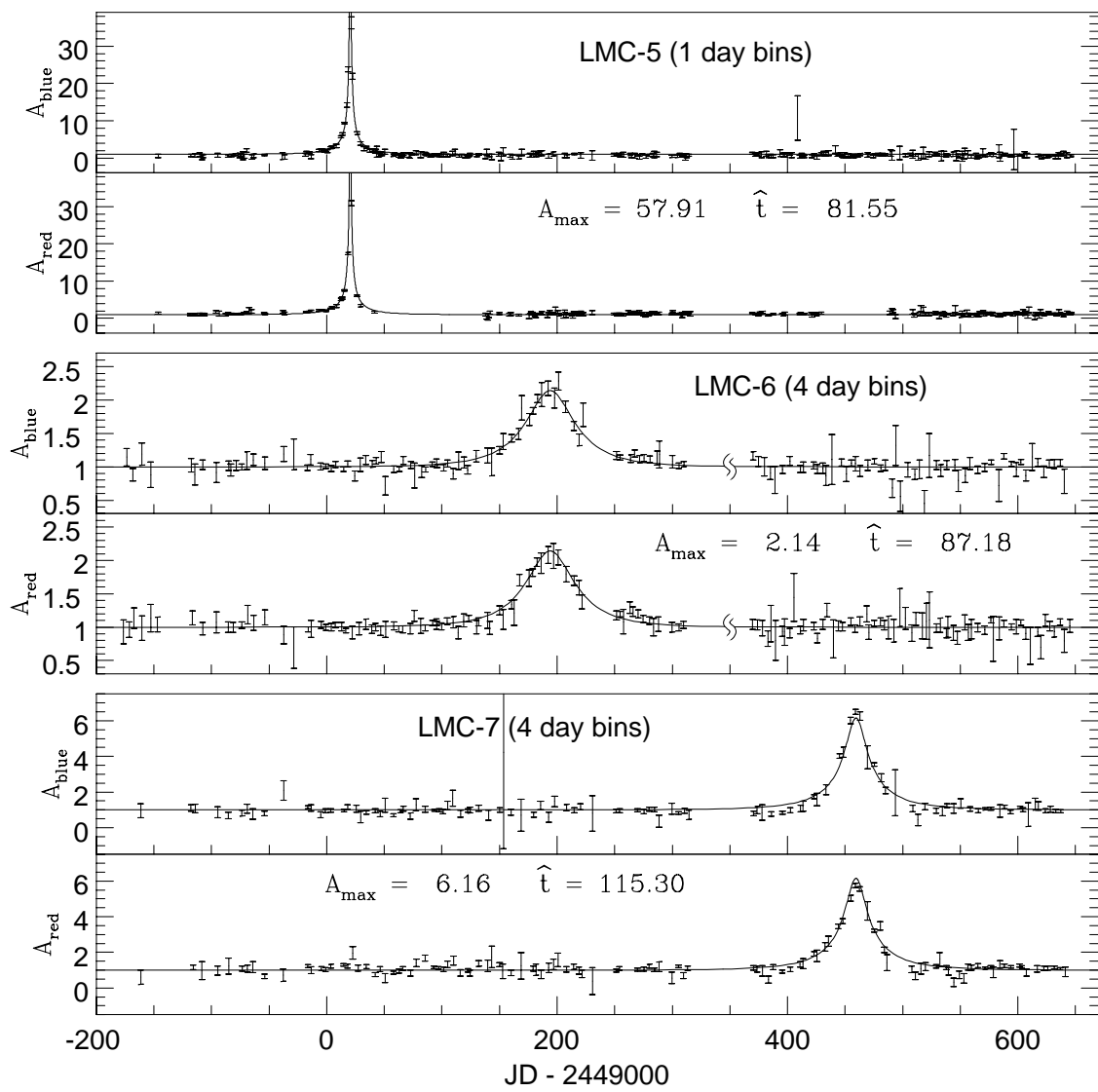


Figure 3 (continued)

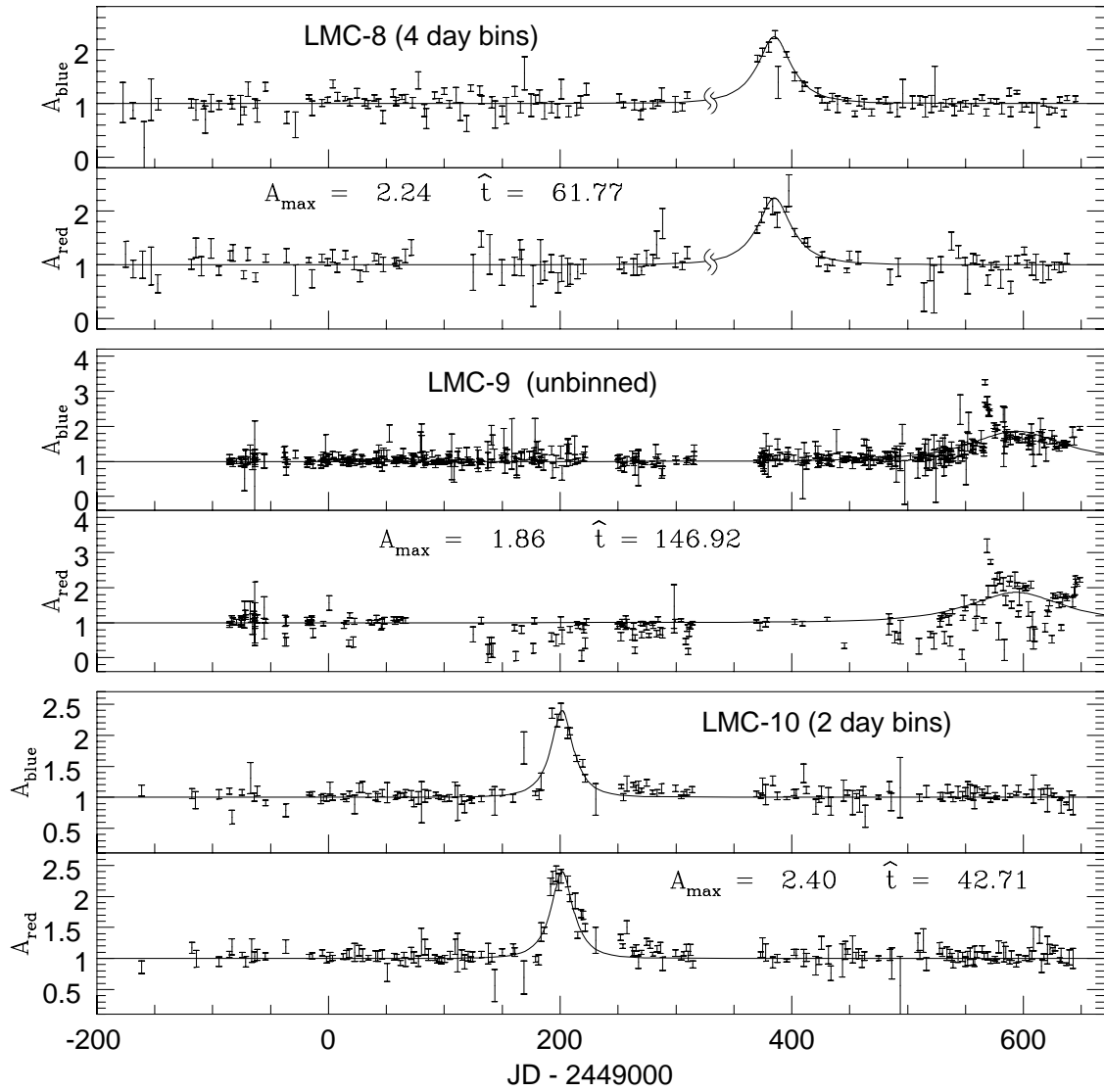


Figure 3 (continued)

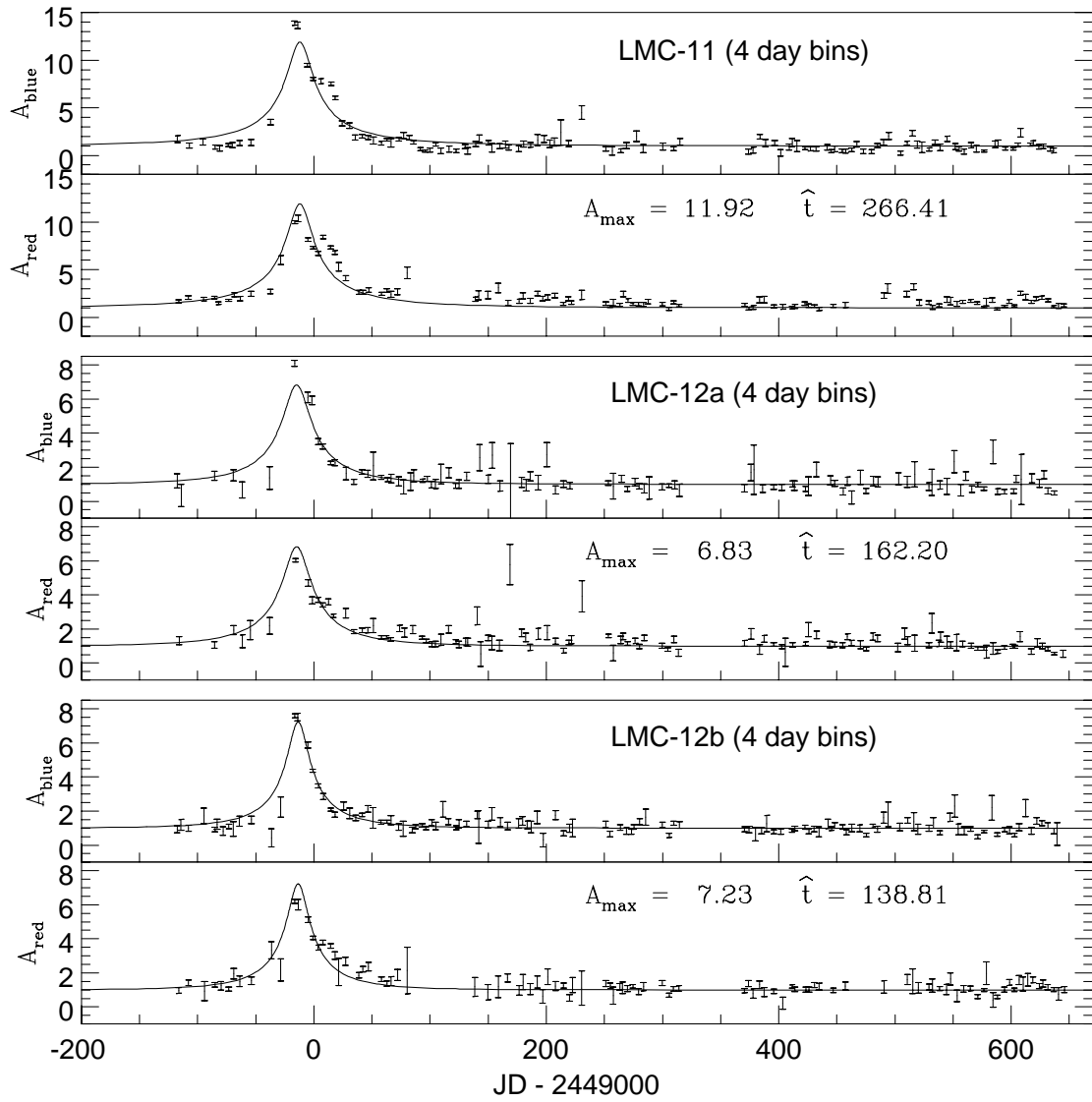


Figure 3 (continued)

Fig. 4.— A mosaic of 2 images centered on each candidate event; the labelled image shows the event near maximum observed brightness, and the un-labelled image shows the event at normal brightness. These are R-band CCD images, with a scale of  $0.63''/\text{pixel}$ . Each box is 40 arcsec square; North is up and East is left.

for the increased frequency of observations during the event. We also obtained photometry from CTIO, and several observers obtained additional photometry and spectra of the star near maximum (Giraud 1994). We classify this as an excellent microlensing candidate.

Event 5 is a very high magnification event ( $A_{\max} \approx 60$ ) in a faint star. Note that this event occurred during the period examined in Alcock *et al.* (1995a) and A96 but did *not* pass the cuts then employed (too crowded and detected color change). Some deviations from the microlens fit are seen in the wings, and the event exhibits clear color variation (see Figure 11). Neither phenomenon is unexpected in such a faint star: there are possible systematic photometry errors due to crowding when the star is near minimum, and the star is very probably blended with another star of different color. This is reflected the substantial improvement in the reduced  $\chi^2$  from 1.680 in the fit without blending to 0.965 in the fit including blending. The symmetry of the lightcurve and the good fit around the peak strongly suggest that this is a microlensing event. We classify this as an excellent microlensing candidate.

Event 6 is a moderate magnification candidate. We classify this as a good microlensing candidate.

Event 7 is a moderately high amplitude microlensing event located well away from the LMC bar. The light curve is quite symmetric, but some small systematic deviations from the fit can be seen in the wings of the light curve. These deviations are probably due to a known systematic error of our photometry code: since stars are fitted in order of descending template brightness, when the seeing is poor the flux from a faint star may be ‘stolen’ by a brighter neighboring star.<sup>13</sup> Once the photometry code has detected a  $> 7\sigma$  deviation brightness variation of a given star, the star and all its close neighbors undergo another iteration of fitting. This reduces the effect of this ‘stolen flux’ problem when the magnification is large. This star also exhibits some color variation that can be explained by blending. We classify this event as a good microlensing candidate.

Event 8 is a moderate magnification microlensing candidate located in the LMC bar. It occurred just after the gap due to the fire, but we still have a reasonable portion of the light curve’s rise. We classify

this as a good microlensing candidate.

Event 9 passes our objective data cuts, but it appears to be quite different from a normal microlensing event. The red baseline data contains a great deal of scatter, but we have determined that this is due to a previously uncatalogued CCD defect: a low level trap that causes images to be smeared across the column with the trap. This defect is responsible for the scattering of low measurements in the red. In an attempt to remove the contaminated observations, we have eliminated all the red observations in which this defect comes within 6 pixels or 1.5 times the image FWHM of the centroid of this star. This procedure should remove most, but probably not all of the photometric contamination due to this CCD defect. The corrected lightcurve of this star is shown in Figure 5. This lightcurve includes data through early 1996, and it was used to obtain a good fit to a binary lens light curve (Bennett *et al.* 1996; Alcock *et al.* 1996e), shown in Figure 6. This fit has a  $\chi^2$  of 1.76 per degree of freedom which is quite typical of other microlensing events. It also requires that a significant amount of the total light comes from an unlensed star in order to obtain a good fit. This is also the case for many of the other binary lensing events which have been observed (Udalski *et al.* 1994b; Alard *et al.* 1995b; Bennett *et al.* 1995a; Pratt *et al.* 1995).

The multiple peaks in the lightcurve with the ‘U-shaped’ structure are quite typical of binary microlensing events (Mao & Paczyński 1991), but would be unexpected for a variable star. In particular, the gradual rise before the first sharp peak would be very unusual for an eruptive variable. We therefore classify this as an excellent microlensing candidate.

The two measurements on the rising portion of the first caustic crossing (the first sharp feature in the event) are potentially very useful. In principle, this will give us an estimate of the angular velocity of the lens and thus a constraint on the location of the lens along the line of sight. Our analysis of this event suggests that the lens is located in the LMC (but note that there are two data points on the caustic crossing). It has been estimated (Bennett *et al.* 1996; Alcock *et al.* 1996e) that there is an a priori probability of about 10% that the source star is also a binary with parameters that would affect the apparent caustic crossing time. The observed caustic crossing time could reflect the time it takes the caustic to cross the orbit of a binary rather than the stellar disk of a single star, so the possibility that this lens system is in

<sup>13</sup>We are currently working in collaboration with P. Stetson to develop an improved photometry code to use on detected events, which should avoid this systematic error.

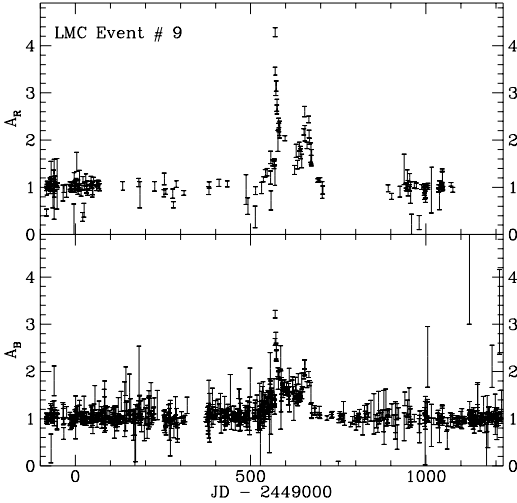


Fig. 5.— The full lightcurve of event 9, including data from additional observations taken after 1994 October. Many of the red data points corrupted by a CCD trap have been removed as described in the text.

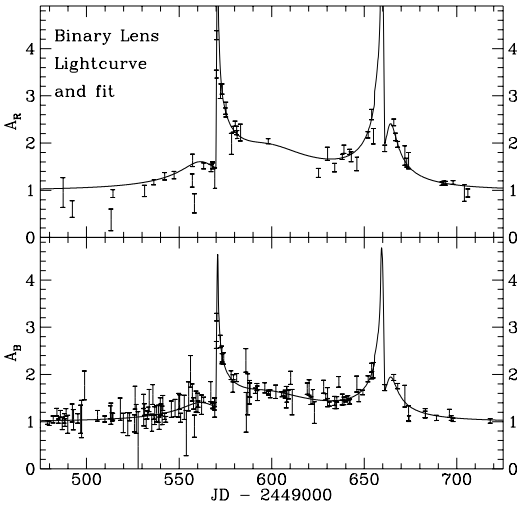


Fig. 6.— Lightcurve of event 9 in the peak region, with the best-fit binary lens lightcurve. Red data points corrupted by a CCD trap have been removed.

the Milky Way halo cannot be ruled out.

Event 10 passes all of our cuts. The asymmetry seen in the light curve, a rapid rise with a more gradual fall, is typical of an eruptive variable star. On the other hand, asymmetric light curves can also arise from binary lensing events and from deviations from the constant velocity assumption. Although event 10 is not close to any of our cut boundaries, we consider it to be our weakest candidate because of the lack of a direct explanation of its light curve asymmetry. If this star is indeed a variable, our experience suggests that it will undergo another outburst in the future. The inclusion or exclusion of this event has little influence on our results. We classify it as a marginal microlensing candidate.

Lightcurves 11 and 12a/b are indicated with open circles in Figure 2 because while they were present in our reference template images, they are now no longer detectable in images that go somewhat deeper. Thus, the unbrightened images of these objects would not have been bright enough for these stars to be detected had we selected template images which were taken later.

Star 11 is superimposed on a background galaxy (see Figure 4) which is at a redshift of 0.021 (spectrum courtesy of J.P. Beaulieu of the EROS collaboration). As noted above, it was invisible on CTIO images to  $V > 22$  in 1995 December. Since obvious galaxies cover a very small fraction of our images ( $< 0.01\%$ ), this is very unlikely to be a chance superposition. The event was almost certainly a supernova in the background galaxy, probably of type II. There is some indication of a plateau or secondary peak about 25 days after maximum. For  $H_0 = 75 \text{ km/sec Mpc}^{-1}$ , it had a peak brightness of about  $M_V \approx -17.5$ .

It is possible that event 12 is actually a microlensing event of a star that is normally below our detection threshold, but since we have only detected this star because it was brighter than normal in our template frame, it is not proper to include it as a microlensing candidate. Our detection efficiency calculations do not allow for lensing of stars which are too faint to have been detected in the template image unless they contribute light to a blended composite object that is above the threshold.

Although events 11 and 12 appear to have significantly positive baseline fluxes in Figure 3, this is due to crowding-related systematic errors, and the presence of the underlying galaxy for event 11. If a star



was present in our template image, our photometry code will estimate its flux in all other images even if it is not significantly detected in them. The points shown in Figure 3 are averages in 4-day bins; most of the individual data points are within  $2\sigma$  of zero flux, but the averaging tends to enhance the apparent significance of the systematic errors.

In summary, we classify events 1, 4, 5, and 9 as ‘excellent’ microlensing candidates, 6, 7 and 8 as ‘good’ candidates, and 10 as a ‘marginal’ candidate. Events 11 and 12 must be rejected as explained above, and events 2 & 3 from A96 do not pass the current cuts.

### 3.3. Comparison with Previous Cuts

It is worth noting that of the above candidates, numbers 1, 5, 6, 10, 11, 12 occurred in the A96 data set. but only event 1 passed the old cuts; we discuss the others below. Event 5 failed cuts on crowding (1) and chromaticity (4) in the year-1 analysis. As noted above, we expect events in faint stars to be somewhat chromatic due to blending, which is why the achromaticity cut has been relaxed. Event 6 failed cuts on a SoDOPHOT object type for individual measurements in the year-1 analysis. This cut was made inadvertently in the year-1 analysis and was corrected after it was noticed in the bulge alert events 95-5 and 95-7<sup>14</sup> (Note that this type cut *was* taken into account properly in the year-1 LMC efficiency calculations.) Event 10 failed year-1 cut (3) on  $\chi_{\text{peak}}^2$  which has been relaxed. Event 11 also failed the year-1 timescale cut (6) as well as the  $\chi_{\text{peak}}^2$  cut, and event 12 failed the year-1 achromaticity cut (4).

Events 10 and 12 were noted by eye as ‘near-miss’ candidates in our previous analysis, but the star and photometry quality cuts were applied at an early stage and so events 5 and 6 were not discovered in the year-1 analysis. Since the lightcurves of events 10, 11 and 12 differ substantially from normal single lens microlensing, it is not surprising that these failed the old cuts; but events 1, 5 and 6 are strong microlensing candidates, and it appears disconcerting that only 1 of these 3 events passed the old cuts. Based on our efficiency estimates below, we would expect the A96 cuts to reject around 15% of single-lens events which pass the new cuts. The binomial probability of  $\leq 1$  ‘success’ out of 3 ‘trials’ given an 85% probability is

$\approx 6\%$ , so this appears unlucky but not unusually so given the small-number statistics.

### 3.4. How Many Events?

The 12 lightcurves that pass our revised event selection criteria represent 10 objects, as two of them (events 1 and 12) occur in field overlap regions and were independently detected. The supernova (event 11) is not microlensing. Event 12 was detected only because of its being magnified above our object detection threshold in the template frame. As our detection efficiency determination does not include this effect, event 12 will be excluded from further consideration.

This leaves a set of 8 apparent events (1 and 4-10), one of which appears to be a binary lens (9), that we will use to estimate the total optical depth towards the LMC. As shown below, the result we obtain exceeds the optical depth expected from known Galactic and LMC populations. It is therefore useful to define a subset of the events that excludes lensing by known objects, as their distribution of timescales contains information about the mass, velocity and spatial distributions of the new lensing population. The difficulty is in choosing which events to include as members of the subsample. Fortunately all the events have, in a broad sense, comparable values of  $\hat{t}$  so the number of events in the subsample is more important than the exact choice of which ones to include.

Given the anticipation of just over one event in the sample from known Galactic and LMC populations, we have elected to construct a somewhat conservative subsample that contains 6 of the 8 events. The binary lensing event (9) was excluded for two reasons: 1) our analysis shows that it may come about from lensing by a binary within the LMC, and 2) it is the longest of the events, and therefore is the most conservative one to exclude. We have also chosen to eliminate event 10 from the subsample. This preserves the average value of  $\hat{t}$  for the two samples. We also think on subjective grounds that it is the weakest of the 8 events. The 6 event subsample containing events 1 and 4-8 is then a reasonable estimate of the events from unknown lensing populations.

### 3.5. Blending Effects

Many of our detected ‘objects’ actually consist of double or multiple stars within the seeing disk. This is unavoidable at the high stellar density in our fields.

<sup>14</sup>Information on MACHO microlensing alerts can be found at URL: <http://darkstar.astro.washington.edu/> on the WWW.

Since the angular Einstein radius is much smaller than the seeing disk, only one star in a blend will typically be lensed; this distorts the observed lightcurve from the shape given in eq. 2. We may model this by adding two parameters to represent the flux of the unmagnified component in each color. Specifically,

$$\begin{aligned} f_R(t) &= f_{uR} + A(t)f_{lR}, \\ f_B(t) &= f_{uB} + A(t)f_{lB}, \end{aligned} \quad (3)$$

where  $A(t)$  is as in eq. 2,  $f_{uB}, f_{uR}$  are the flux of the unlensed component in each passband, and  $f_{lB}, f_{lR}$  are the baseline flux of the lensed star in each passband. We use instrumental flux units which roughly correspond to 100 detected photo-electrons in a 300 second exposure.

The results of these fits are shown in Table 4; we see that for events 1, 6, 8, 10 the best fit is quite close to the unblended case, while for events 4,5 and 9 the best fit contains substantial blending. This is important because blending causes a significant change in the parameters; if an event exhibits significant blending, the single-lens fit will systematically underestimate  $A_{\max}$  and  $\hat{t}$  relative to the true values. Clearly, we can correct for this effect by using the blend fit values for  $\hat{t}$  when we calculate the microlensing optical depth or the most likely lens mass. These  $\hat{t}$  values are the most accurate estimate of the true  $\hat{t}$  value for each event, but we are concerned that small systematic errors in our photometry might cause us to systematically overestimate  $\hat{t}$ . Therefore, we have chosen a less accurate, but unbiased method for estimating  $\hat{t}$ . We use the  $\hat{t}$  values from the unblended fits and then apply a statistical correction to each of our observed  $\hat{t}$ 's. This average correction has been determined from our Monte Carlo simulations, and the resulting values are shown in Table 7. This technique works for all events except for the binary event which was not represented in our Monte Carlo calculations. The blended, binary lens fit  $\hat{t}$  value is used for this event.

We previously imposed the condition that there be no color variation in a microlensing event (Alcock *et al.* 1993, 1994, 1995a; A96). A convenient graphical illustration of the color test is a plot of  $f_R(t)/f_B(t)$  versus time (Alcock *et al.* 1993). Event 1 shows no variation of this flux ratio with time (Alcock *et al.* 1993). Event 5, however, would show clear color variation. One virtue of this graphical presentation is that the test is independent of the magnification  $A(t)$ .

Eq. 3 suggest an obvious generalization. A plot

of  $f_B(t)$  versus  $f_R(t)$  should be a straight line. This should be true for any functional form of  $A(t)$ , and can be applied equally to single, binary, or more general microlensing events as long as the multi-color measurements are simultaneous. Figure 7 shows these plots for our 8 candidate events. There is no evidence for systematic deviation from straight line behavior in any of these plots. The straight lines plotted in Figure 7 are derived from the best fit of eq. 3 to each event.

#### 4. Detection Efficiency

In order to draw quantitative conclusions, we clearly need reasonably accurate knowledge of our detection efficiency. The detection probability for individual events depends on many factors, e.g. the 3 event parameters  $A_{\max}, \hat{t}, t_{\max}$ , and the unlensed stellar magnitude, as well as our observing strategy and weather conditions. However, we can average over the known distributions in  $A_{\max}$  and  $t_{\max}$  and stellar magnitude, using the known time-sampling and weather conditions, to derive our efficiency as a function only of event timescale  $\mathcal{E}(\hat{t})$ .

We have computed our detection efficiency using an essentially identical method to that outlined in A96, simply generating simulated microlensing events with  $\hat{t}$  logarithmically distributed in the range 0.3–1000 days over the wider time interval, JD – 2,449,000 = –176.5 to 663.5, and adding these simulated events into the extended timespan of observations. The Monte-Carlo procedure takes into account the actual spacing and error bars of the observations, so any variations in sampling frequency, weather, seeing etc. between the first and second year data are automatically accounted for.

There are two levels of detail in these calculations; firstly a ‘sampling’ efficiency, in which we neglect stellar blending and assume that all the additional flux in a microlensing event is recovered by the photometry code; and secondly a ‘photometric’ efficiency, where we add artificial stars to a representative set of real images, re-run the photometry code and create look-up tables of added vs. recovered flux. These look-up tables are then used to generate artificial microlensing lightcurves in the same way as above. This ‘photometric’ efficiency is more realistic, and is typically  $\sim 20\%$  lower than the ‘sampling’ efficiency for timescales less than 200 days.

The photometric efficiency is based on all stars in

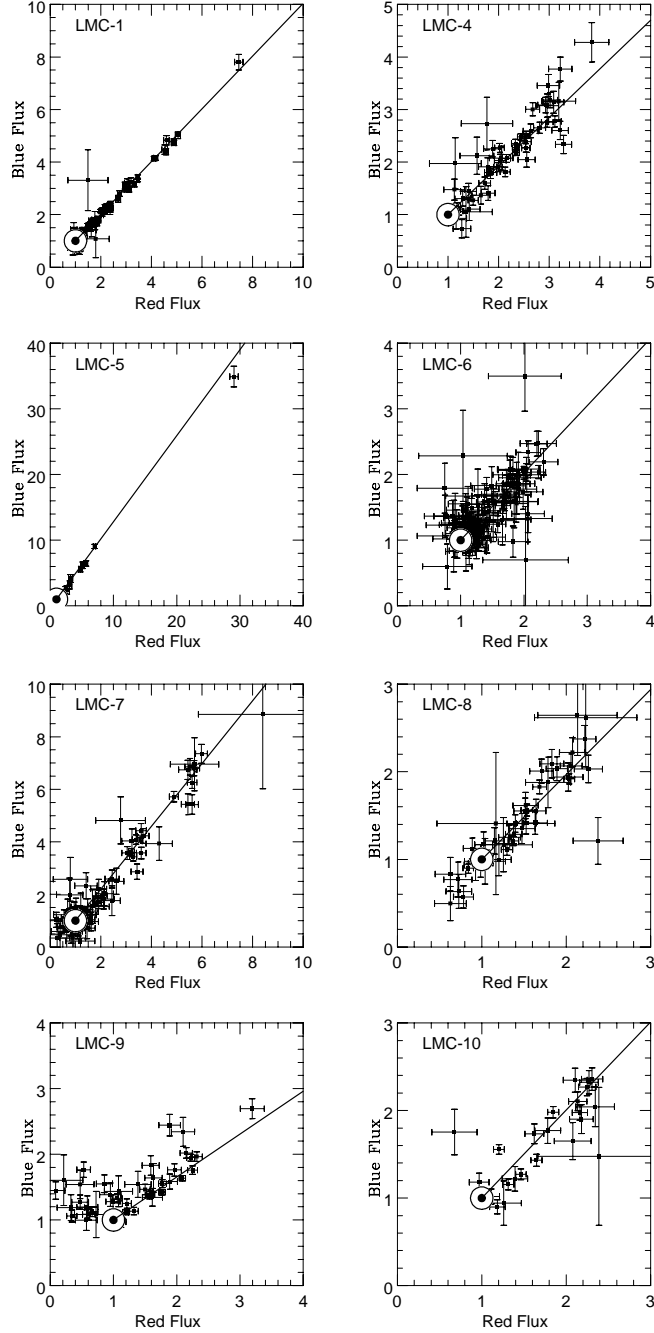


Fig. 7.— The blue flux is plotted against the red flux for all the simultaneous measurements within  $1 \hat{t}$  for all of the events passing our microlensing cuts. The solid lines indicate the flux ratios predicted by the blended microlensing fits listed in Table 4.

our fields, even those not uniquely identified because of S/N or crowding effects. These are accounted for by integrating the detection efficiency per star over a corrected luminosity function (LF) as in A96. This corrected LF is truncated about one magnitude beyond where our measured LF becomes seriously incomplete. However, the real LF continues to rise as  $10^{0.5m}$  for several magnitudes ( $m$ ) beyond this cutoff so there should be an additional contribution to our exposure from these fainter stars. We have tried several different magnitude cutoffs and it appears that our exposure is converging near or below the cutoff used in this paper for events with  $\hat{t} < 150$  days. Any additional contribution should be relatively insignificant for reasons discussed in the appendix.

Efficiency results are shown in Figure 8. We define our efficiency as the fraction of input events with  $u_{\min} < 1$  which pass our cuts; since we use a cut of  $A_{\max} > 1.75$  or  $u_{\min} < 0.661$ , our efficiency is constrained to be less than 0.661. This efficiency is defined relative to an ‘exposure’ of  $E = 1.82 \times 10^7$  star-years, which arises as follows: there are 9.2 million lightcurves in our total sample, of which 8% have insufficient valid data points to be used in the simulations, and 6.5% occur in field overlaps. The relevant timespan is the 840-day interval over which we add the simulated events; thus the exposure is  $7.9 \times 10^6$  stars  $\times$  840 days =  $1.82 \times 10^7$  star-years.

The efficiency for timescales  $\hat{t} \sim 10 - 60$  days is lower than that from A96 by  $\sim 10\%$ ; this is because we gain around 10% from loosening the goodness-of-fit and star quality cuts, but we lose about 20% from the tighter  $A_{\max}$  and  $\Delta\chi^2$  cuts. A more operational comparison of the 1-year and 2-year samples is seen in Figure 9 which shows ‘effective exposure’  $E\mathcal{E}(\hat{t})$ .

The most substantial difference occurs at long timescales, where the ‘new’ efficiency is significantly higher than in A96. This occurs partly as a consequence of the longer timespan which allows longer events to fit within our observing window; and partly because we have relaxed the year-1 cut  $\hat{t} < 250$  days,  $t_{FWHM} < 100$  days to simply  $\hat{t} < 300$  days. The main motivation for the  $t_{FWHM} < 100$  days cut was to give a second redundant cut, in addition to the positional cut, to reject the clump of ‘nebosity variables’ in 30 Dor, which we earlier suspected to be T Tauri stars. These events have now been recognized as arising from the light echo around SN 1987A (c.f. Xu, Kunkel & Crots 1995); they seem to arise from small ‘knots’ of nebosity illuminated by the light

echo, hence the smearing of the echo by the light-crossing time results in roughly symmetrical brightening events for some of these objects. Since we know that there have been no other LMC supernovae in recent years, we can simply reject all candidate events from this small patch of sky, and the timescale cut can be relaxed.

There are a number of shortcomings of the present efficiency analysis. One problem is that the luminosity function used for the simulated events in the efficiency analysis does not go as deep as we would like. We are not very sensitive to short timescale events for very faint stars, so our truncation of the luminosity function is not a problem, but for longer timescale events we get significant detection probabilities at faint magnitudes. For  $\hat{t} > 200$  days it appears that there may be a significant contribution to the overall detection probability from stars fainter than the ones we have included in our efficiency calculations, so our ‘photometric’ efficiency is probably an underestimate for these long events. For detected events with  $\hat{t} < 75$  days, we expect that the systematic error in our ‘photometric’ efficiency due to the truncated Monte Carlo LF is less than 5%. For events with  $\hat{t} < 150$  days this error is expected to be less than 10% of our final efficiency values.

The efficiency determination also depends upon how well the Monte Carlo simulations represent realistic distributions of microlensing events. The main shortcoming of our Monte Carlo simulations is that all events are assumed to be “normal” microlensing events with a single lens, a point source, and constant velocities. There are, of course, observed microlensing events (such as event 9) which violate these assumptions, and our detection efficiency estimates are clearly overestimates of our actual efficiency of detecting these exotic lensing events. This will cause our efficiencies to be overestimated perhaps by as much as 5%. (The factor may be larger than this for the year-1 analysis which relied more heavily on fit  $\chi^2$  cuts than the present analysis does.) Since two main shortcomings of our efficiencies have opposite signs and magnitudes of 10% or less, we feel that the total systematic error in our efficiencies is probably less than 10%. A somewhat more conservative estimate of the systematic efficiency error is just the difference between the photometric and sampling efficiencies which is about 15% for events with timescales in the observed range.

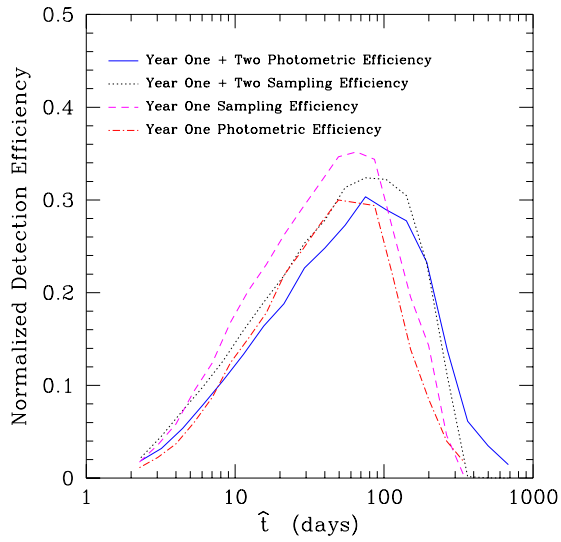


Fig. 8.— Microlensing detection efficiency (normalized to  $u_{\min} < 1$ ) for the 2-year Macho data, as a function of event timescale  $\hat{t}$ . The dotted line shows the ‘sampling’ efficiency, and the solid line shows the ‘photometric’ efficiency as described in § 4. For comparison the corresponding curves from year-1 (A96) are shown.

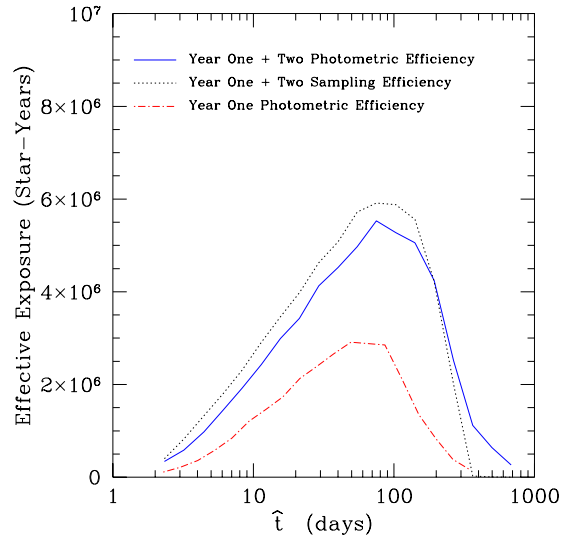


Fig. 9.— ‘Effective exposure’  $E\mathcal{E}(\hat{t})$  to microlensing (normalised to  $u_{\min} < 1$ ) for the 2-year Macho data. The solid line is the best estimate using ‘photometric’ efficiency; the dotted line is an upper limit using ‘sampling’ efficiency. For comparison, the dot-dash line shows the value for the 1-year analysis using the “photometric” efficiency.

## 5. Event Distributions

There are a number of statistical tests that can be performed on microlensing event distributions to test the hypothesis that our events are indeed gravitational microlensing, or to test hypotheses regarding the lens population. With only 8 events, these tests are not conclusive, but they do support the interpretation that we have observed gravitational microlensing by a new population.

### 5.1. Impact Parameters

An important model independent test of the hypothesis that we have observed gravitational microlensing is to compare the distribution of peak magnifications to the theoretical prediction. It is convenient to switch variables from the maximum magnification ( $A_{\max}$ ) to the minimum distance of approach between the Macho and the line of sight, in units of the Einstein radius,  $u_{\min} = b/r_E$ . Events should be uniformly distributed in  $u_{\min}$ ; this distribution is then modified by the experimental detection probability which is higher for small  $u_{\min}$  (high  $A_{\max}$ ). This comparison was previously performed with a larger sample of bulge events and the data were found to be consistent with the microlensing hypothesis (Alcock *et al.* 1996b). The observed and predicted distributions for our LMC events are shown in Figure 10; a KS test shows a probability of 96.6% of getting a KS deviation worse than the observed value 0.177. (The binary event 9 is excluded from this comparison because the dependence of the detection efficiency on  $u_{\min}$  is substantially different for binary events.) We conclude that the distribution of events in  $u_{\min}$  is consistent with the microlensing interpretation.

The  $u_{\min}$  distribution and the high magnification events may be used to lend support to the interpretation of our lower magnification events. The higher magnification events are striking, and are clearly separated from the background in Figure 2. They are distinct from any known type of intrinsic stellar variability, so they are very likely to be lensing events. Microlensing predicts a uniform distribution in  $u_{\min}$  (with a slight modification due to nonuniform detection efficiency), so we expect that (at least) some of the lower magnification events must also be caused microlensing.

This argument can be made quantitative. Consider the event subsets  $\{1,5\}$ ,  $\{1,5,7\}$ , and  $\{1,4,5,7\}$ . These sets contain the highest 2, 3, and 4 magnification

events respectively. For each subset of  $n$  events, we evaluate the mean  $u_{\min}$  value:  $\langle u_{\min} \rangle$ . We then use a Monte-Carlo simulation using the efficiency-corrected  $u_{\min}$  distribution from Section 4 to compute the probability that a sample of  $n$  events will have a  $\langle u_{\min} \rangle$  value as small as the observed value. For example,  $\langle u_{\min} \rangle = 0.080$  for events 1 & 5, but only 3.2% of simulated 2 event data sets have  $\langle u_{\min} \rangle$  values this small. Thus, it is unlikely that events 1 and 5 are the *only* microlensing events which pass our cuts, so at least one of the other events should also be microlensing. Table 5 shows the results of this test for a number of different data subsets. This table indicates that it is also unlikely that the 3 or 4 highest magnification events are the *only* real microlensing events which pass our cuts. When we consider event subsets which include one or more of the events with  $A_{\max} < 2.5$ , then the  $\langle u_{\min} \rangle$  values are much closer to the expected value of  $\langle u_{\min} \rangle = 0.310$ . In particular, the set of all non-binary microlensing candidates,  $\{1, 4-8, 10\}$ , and the set of all non-binary events classified as excellent or good microlensing candidates,  $\{1, 4-8\}$ , both give quite acceptable values for  $\langle u_{\min} \rangle$ . If we consider the set of non-binary ‘excellent’ microlensing candidates,  $\{1, 4, 5\}$ , we find that their  $\langle u_{\min} \rangle$  is marginally incompatible (at the 90% c.l.) with the hypothesis that they are the only microlensing events to pass our cuts. Thus, when we add in the binary event (which is classified as excellent) we find that the  $\langle u_{\min} \rangle$  test indicates that at least 5 of our microlensing candidates are likely to be actual microlensing events. If the “5th” real microlensing event is event 7, then the set of non-binary candidates  $\{1, 4, 5, 7\}$  still have an unexpectedly small value of  $\langle u_{\min} \rangle$ . Thus, if the number of real lensing events is  $< 6$ , then it is probably the case that event 7 which has a symmetric lightcurve with  $A_{\max} \approx 6$  is a variable star of a previously unknown class. The microlensing interpretation seems more likely than this.

## 5.2. Color-Magnitude Diagram

The gravitational microlens does not distinguish between types of star. The stars which have undergone microlensing should be “democratically” distributed over the color magnitude diagram for the LMC. Figure 11 shows a color magnitude diagram with each of the 8 microlensing candidates along with all the stars in a  $5' \times 5'$  region around each candidate. Most of the events are along the faint main sequence where most of the observed LMC stars reside. Using the Monte Carlo simulations that were run to determine our microlensing event detection efficiencies, we have computed the fraction of lensing events in which the source star appears to be a clump giant star (the clump giants are defined for this purpose by the box indicated in Figure 11). For events with timescales of  $\hat{t} \approx 75$  days, this fraction is 10% which is quite consistent with the 1 of our 8 events which resides in the clump. Event 5 appears to lie in a sparsely populated region of the diagram, but this is because the magnified star (which lies on the main sequence) is blended with a much redder object. We conclude that the distribution of events is not clustered in the color magnitude diagram and is consistent with the microlensing interpretation.

## 5.3. Spatial Distribution

For microlensing by Machos smoothly distributed in the Galactic halo, we expect the detected events to be distributed across our fields in proportion to the local exposure,  $E$ . In contrast, models in which LMC objects dominate the lensing population predict that the lensing events will be concentrated within the LMC bar (Wu 1994; Sahu 1994).

Figure 1 indicates that the detected events are apparently spread evenly across our 22 fields. To quantify this impression, we consider a simple model for the LMC bar: the bar is an ellipse with semi-major axis of 70 arcmin and axis ratio 4:1. We define a “distance” of a point from the center of the bar to be the semi-major axis of a similar ellipse which passes through that point. We consider the expected distribution of events over this distance from the bar, under three models: (1) the microlensing optical depth does not vary over our fields (pure Galactic halo microlensing); (2) the microlensing optical depth is 4 times greater inside the bar than outside (large contribution from LMC lenses); and (3) the microlensing optical depth is 12 times greater inside the bar than

outside (huge contribution from LMC lenses). Models (2) and (3) bracket the models proposed by Sahu (1994) who suggested that the microlensing optical depth inside the bar should be 4-12 times larger than the optical depth outside the bar. The cumulative distributions of bar distances resulting from Monte Carlo realizations of these three models are compared with our 8 and 6 events samples in Figure 12.

We use non-parametric statistical tests to quantify the match of the observations to the models. Specifically, we have used one- and two-sided Kolmogorov-Smirnov tests and the Wilcoxon two sample test (Kendall & Stuart 1988). This latter test utilizes only the rank ordering of the data and is especially powerful for testing whether one distribution is systematically shifted from another. As we apply this test, the null hypothesis is that the distributions of bar distances are identical between model and observation, while the alternative hypothesis is that the bar distances for the observations are greater than those for the model. The probability of the null hypothesis is given for each model in Table 6. We note that as this probability decreases, the likelihood that the model is correct decreases.

The results show that the most extreme LMC lens model is ruled out at roughly a 90% confidence level by the most powerful statistical tests, with the less extreme being ruled out at only about 70% confidence. Clearly, this result is not yet conclusive, but with the additional data that will be available within a few years, it should be possible to determine whether or not LMC microlensing makes a significant contribution to the total.

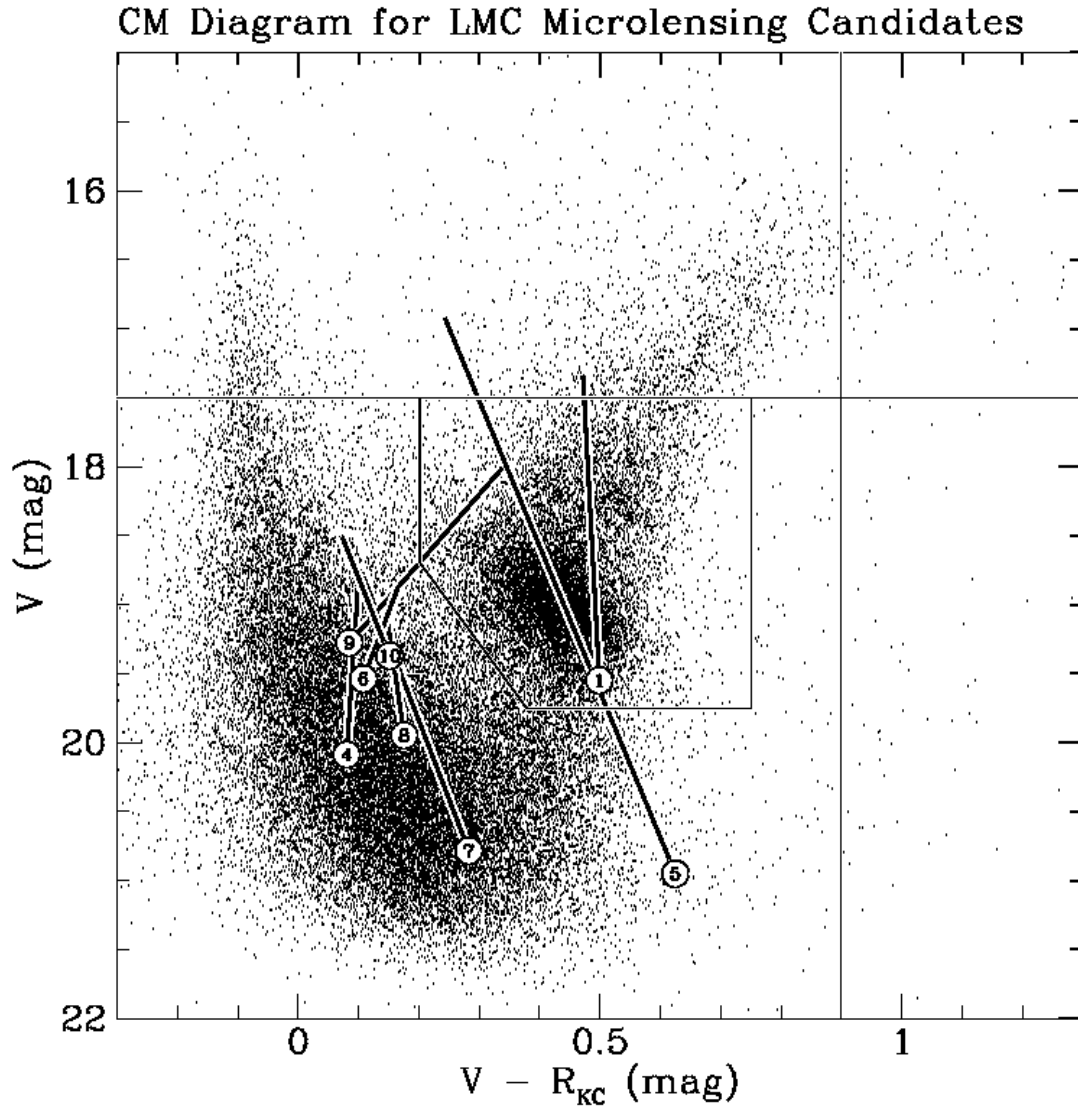


Fig. 11.— The locations of the 8 candidate microlensing events on the color-magnitude diagram. The events at normal brightness are shown as numbered circles, with bars indicating their locations at peak brightness. The small dots show all stars from a  $5' \times 5'$  box around each event. The regions of the color-magnitude diagram which are excluded from the microlensing search ( $V > 17.5$  and  $V - R > 0.9$ ) are indicated with straight lines, and the “giant branch region” is indicated by the closed figure.



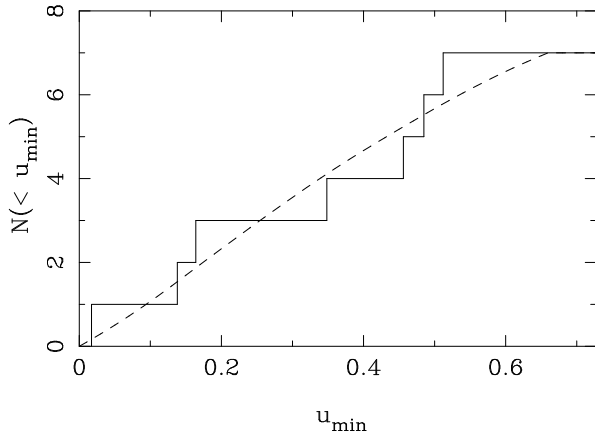


Fig. 10.— The solid line shows the cumulative distribution in  $u_{\min}$  of 7 candidate events (excluding the binary event 9). The dashed line shows the expected distribution, i.e. a uniform distribution modified by our efficiency.

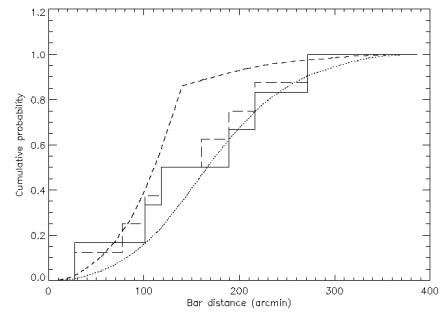


Fig. 12.— Cumulative distributions of the “distances” of the events from the center of the LMC bar are shown for the 8 and 6 event samples (long dashed and solid curves respectively) as well as for the “pure halo lensing” (dotted curve) and the extreme bar lensing models (short dashed curve).

## 6. Implications

In this section we examine the consequences of the observed candidate microlensing events for the dark matter in the Milky Way. We start with the inferred microlensing optical depth, which is compared with the optical depth expected from a “standard” dark halo comprised entirely of Machos. We discuss the sensitivity of our conclusions to the detection efficiencies, and to the selection criteria. We then discuss the observed microlensing rate, and the durations of the events we have seen. We are able to obtain a plausible estimate of the total mass in Machos, and to place a strong upper bound on the contribution of low mass Machos. We employ maximum likelihood estimators to infer typical masses and probable Macho fractions for various model halos. Finally, we discuss the possibility that some or many of our observed events arise from objects not in the dark halo of the Milky Way.

### 6.1. Optical Depth Estimates

The simplest measurable quantity in a gravitational microlensing experiment is the microlensing optical depth, which is defined to be the instantaneous probability that a random star is magnified by a lensing object by more than a factor of 1.34. This is related to the mass in microlensing objects along the line of sight to the source stars by

$$\tau = \frac{4\pi G}{c^2} \int \rho(l) \frac{l(L-l)}{L} dl \quad (4)$$

Thus, it depends only on the density profile of lenses, not on their masses or velocities. Experimentally, one can obtain an unbiased estimate of the optical depth as

$$\tau_{\text{meas}} = \frac{1}{E} \frac{\pi}{4} \sum_i \frac{\hat{t}_i}{\mathcal{E}(\hat{t}_i)}. \quad (5)$$

where  $E$  is the total exposure (in star-years),  $\hat{t}_i$  is the Einstein ring diameter crossing time, and  $\mathcal{E}(\hat{t}_i)$  is the detection efficiency. Here, and below, we use the average blend corrected values of  $\hat{t}_{bl}$  from column 3 of Table 7. These take into account the fact that our typical star is blended, and so the fit  $\hat{t}$  is typically underestimated. As above, our total exposure is  $E = 1.82 \times 10^7$  star years.

It is also convenient to define the function

$$\tau_1(\hat{t}) = \frac{1}{E} \frac{\pi}{4} \frac{\hat{t}}{\mathcal{E}(\hat{t})}, \quad (6)$$

which is the contribution to  $\tau_{\text{meas}}$  from a single observed event with timescale  $\hat{t}$ .  $\tau_1$  values for each of our events are also listed in Table 7. Confidence levels on our measured value of  $\tau_{\text{meas}}$  are determined with the following procedure. We consider sets of events chosen according to Poisson statistics with event timescales randomly selected from the observed set of timescales. The Poisson distribution has a parameter, the number of events expected ( $N_e$ ), which is adjusted so that some fixed fraction of the generated data sets (say, 16%) have ‘measured’ optical depths that are larger than our actual value of  $\tau_{\text{meas}}$ . The mean optical depth for the selected value of  $N_e$  is then selected as the confidence limit value. (In our example, the confidence level would be 16%—or a 1- $\sigma$  lower limit on  $\tau_{\text{meas}}$ .) Our results for  $\tau_{\text{meas}}$  and confidence intervals are shown in Table 8. As explained below, this procedure can underestimate the errors when events much longer than those detected are not highly unlikely, but it gives a reasonable estimate for the lower limit on  $\tau_{\text{meas}}$ .

Using our full sample of 8 events, we find an optical depth for events of duration 2 days  $< \hat{t} < 200$  days of  $\tau_2^{200} = 2.9_{-0.9}^{+1.4} \times 10^{-7}$ . If we subtract the predicted background microlensing optical depth of  $\tau_{\text{backgnd}} = 0.5 \times 10^{-7}$  (from Table 10 below), we find that the observed excess is about 50% of the predicted microlensing optical depth for a “standard” all-Macho halo of equation 8 below. Alternatively, we can estimate the optical depth due only to the halo by using the 6 event subsample defined in section 3.2, for which  $\tau_2^{200} = 2.1_{-0.7}^{+1.1} \times 10^{-7}$ , about 45% of the optical depth predicted by a “standard” all-Macho halo.

This optical depth estimate has the virtue of simplicity; however, since the events are “weighted”  $\propto \tau_1$ , it is hard to assign meaningful confidence intervals to  $\tau$  without assuming some particular  $\hat{t}$  distribution. This is illustrated in Figure 13, which shows the contribution to the sum in eq. 5 from events in various bins of  $\hat{t}$ . Within each individual bin, the events have similar ‘weights’ and the uncertainties are well approximated by Poisson statistics. The confidence intervals in Fig. 13 are derived as follows: for each bin, we derive upper and lower limits  $N_{\text{up}}, N_{\text{lo}}$  on the expected number of events in the bin in the usual way, from the observed number of events in the bin and Poisson statistics. Then, we evaluate the maximum and minimum contribution to  $\tau_{\text{meas}}$  from a single hypothetical event in the timescale bin, i.e.  $\tau_1^{\text{min}} = \min(\tau_1(\hat{t}); \hat{t} \in \text{bin})$  and likewise for  $\tau_1^{\text{max}}$ .

This gives limits  $\tau_{\text{lo}} = N_{\text{lo}}\tau_1^{\text{min}}$  and  $\tau_{\text{up}} = N_{\text{up}}\tau_1^{\text{max}}$  for each bin, which are actually somewhat conservative.

This figure illustrates two important points: firstly, the absence of short events with  $2 < \hat{t} < 30$  days places strong upper limits on the optical depth from events in this interval. Although the efficiency is smaller here, an observed event would contribute  $\tau_1(\hat{t}) \propto \hat{t}_i/\mathcal{E}(\hat{t}_i)$  which is small. Thus, the effective ‘‘sensitivity’’ of the experiment, in terms of number of detected events per unit optical depth, is proportional to  $\mathcal{E}(\hat{t})/\hat{t}$ , **not** just  $\mathcal{E}(\hat{t})$ . This function is maximal at around  $\hat{t} \sim 7$  days.

Secondly, the uncertainties become very large at longer timescales, due to the combination of increasing  $\hat{t}$  and decreasing  $\mathcal{E}(\hat{t})$ . Thus the overall uncertainty in  $\tau$  is considerably greater than simple Poisson statistics based on 6 or 8 events. For example, if we should expect to have observed on average 1 additional event with  $\hat{t} \sim 300$  days, but we happened to observe no such event, the real  $\tau$  would be  $2\times$  the above estimate, and we clearly cannot exclude such a possibility with any confidence. Thus, it is dangerous to quote any optical depth result as an ‘upper limit on Machos’ without specifying a mass or timescale interval to which this limit applies.

## 6.2. Optical Depth Efficiency Dependence

Table 8 includes a number of estimates in addition to our best estimate of the optical depth confidence levels, which is given in bold face type and uses the photometric efficiency with the average  $\hat{t}$  corrections. While the photometric efficiency is the best estimate of our detection efficiency, it is a slight underestimate of our detection efficiency for ‘normal’ (single lens, constant velocity) events because we have not included the contribution due to very faint stars as explained above. This leads toward a slight underestimate of  $\mathcal{E}$ , while our efficiency for detecting exotic microlensing events has been overestimated. Thus, there are two known systematic efficiency errors which tend to cancel. To get some idea how much these problems might affect our optical depth calculations, we have calculated  $\tau_{\text{meas}}$  using the sampling efficiencies which are expected to be overestimates of the true detection efficiencies for events in the range  $20 \text{ days} < \hat{t} < 150 \text{ days}$ . Thus, we expect that the sampling efficiency  $\tau_{\text{meas}}$  confidence levels given in Table 8 are likely to be underestimates of the true microlensing optical depth.

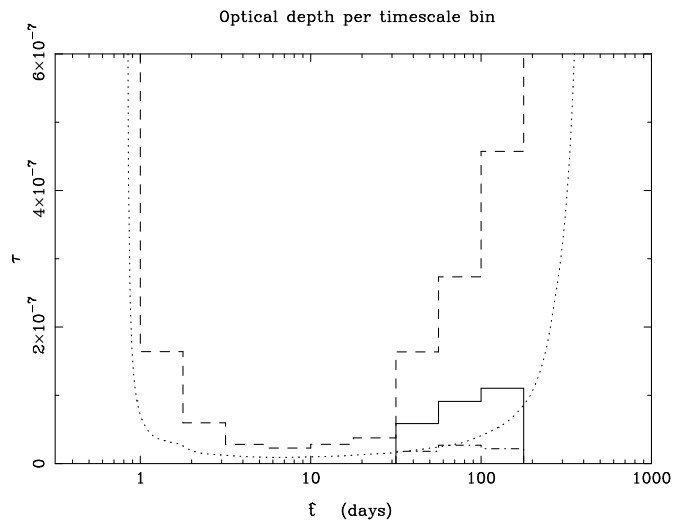


Fig. 13.— The contribution to the optical depth of eq. 5 from events binned in timescale. The solid line shows the observed values from the 8-event sample; the dashed and dot-dash lines show the 90% confidence upper and lower limits (see text). The dotted curve shows the contribution to  $\tau$  which would arise from a single observed event with timescale  $\hat{t}$ .

Another variation of our  $\tau_{\text{meas}}$  values that are shown in Table 8 is due to our choice between  $\hat{t}$  correction methods due to blending. We have used the average  $\hat{t}$  corrections given in Table 7 for our ‘official’ results, but another choice would be to use the blend fit values given in Table 4. The blend fit values are certainly more accurate on an event-by-event basis, but we are concerned that they might tend to systematically overestimate the true  $\hat{t}$  value. As shown in Table 8, this choice has little effect on our results.

Also included in Table 8 are two lines using sampling efficiencies with *no*  $\hat{t}$  correction at all. This is likely to give rise to a substantial underestimate of  $\tau_{\text{meas}}$ , but we include it because (as discussed above) it gives a firm lower limit on  $\tau_{\text{meas}}$ . A reasonable estimate of our  $1\text{-}\sigma$  systematic error in our efficiency determination is given by the scatter of all the  $\hat{t}$  corrected values listed in Table 8. This is about 10% which is much smaller than the statistical errors.

The last two rows of Table 8 give confidence limits on  $\tau$  for the 6 event subsample. These are included to allow the reader to assess the effect of removing some of the selected events from the sample. Event 10, for example, has a lightcurve asymmetry that resembles that of a variable star. If we remove this event, and the longest event (event 9), we have our 6 event sample. Table 8 indicates that even with 6 event sample and the upper limit efficiencies (*i.e.*, sampling efficiencies with *no*  $\hat{t}$  correction), the 97.5% confidence level lower limit on the microlensing optical depth is still larger than total microlensing optical depth of  $\tau_{\text{background}} = 0.54 \times 10^{-7}$  given in Table 10 below. Thus, the excess microlensing optical depth over the background prediction is not sensitive to the uncertainties in our microlensing detection efficiencies or to the possibility that a small fraction of our candidate microlensing events might actually be variable stars.

### 6.3. Optical Depth Cut Dependence

Figures 14 and 15 show the dependence of the measured optical depth on the  $u_{\text{min}}$  and  $\Delta\chi^2/(\chi_{ml}^2/N_{\text{dof}})$  cuts. The heavy curves indicate  $\tau_{\text{meas}}$  for the full 8 event sample while the light curves give  $\tau_{\text{meas}}$  for the 6 event subsample. For the binary event we have assigned a  $u_{\text{min}}$  value of 0.609 which is the value obtained for the single lens fit. Another option would have been to use the binary fit value of  $|u_{\text{min}}| = 0.054$ . This is not appropriate, however, because the binary fit includes blending whereas our cut used the unblended single lens fit value. Strictly speaking, the

single lens fit value would be correct if we had used a binary event detection efficiency in order to calculate the binary event’s contribution to  $\tau_{\text{meas}}$ .

We have also adjusted the  $\Delta\chi^2/(\chi_{ml}^2/N_{\text{dof}})$  values used in Figure 15 for the binary event and the alert event (event 4). For the binary event  $\Delta\chi^2 = 7191$  while  $\chi^2/N_{\text{dof}} = 6.868$  for the single lens fit and  $\chi^2/N_{\text{dof}} = 1.755$  for the binary lens fit. For Figure 15 we have used the binary fit value of  $\chi^2/N_{\text{dof}}$  implying  $\Delta\chi^2/\chi_{ml}^2/N_{\text{dof}} = 5018$  for the binary event. The alert event was detected in progress substantially before peak magnification, and this resulted us obtaining more observations than normal of field 13 (which includes this star). We have taken up to 4 observations of field 13 per night when we would normally have taken only 1 or 2. Thus, for event 4,  $\Delta\chi^2/(\chi_{ml}^2/N_{\text{dof}}) = 6728$  is larger than we would get with our normal observing strategy by a factor of  $\sim 3$ . Therefore, we have reduced the value of  $\Delta\chi^2/(\chi_{ml}^2/N_{\text{dof}})$  used for event 4 in Figure 15 to 2243.

Figures 14 and 15 clearly indicate that our optical depth results are not very sensitive to our choices of cut values. The  $\tau_{\text{meas}}$  values generally do not vary by more than the  $1\text{-}\sigma$  statistical error bars for  $u_{\text{min}}$  and  $\Delta\chi^2/(\chi_{ml}^2/N_{\text{dof}})$  cuts in the ranges  $0.1 \leq u_{\text{min}} \leq 0.661$  and  $500 \leq \Delta\chi^2/(\chi_{ml}^2/N_{\text{dof}}) \leq 5000$ .

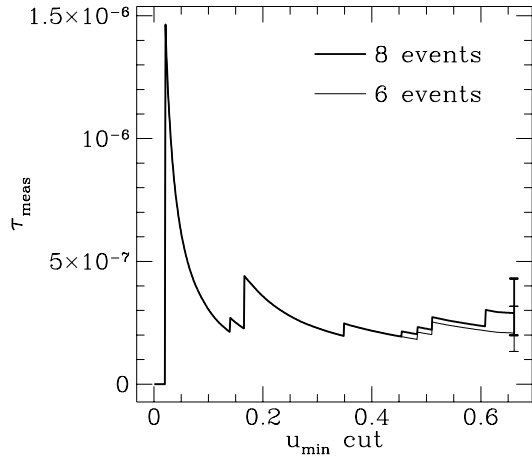


Fig. 14.— The measured microlensing optical depth is plotted as a function of the  $u_{\min}$  cut for the 8 event sample (thick line) and the 6 event ‘halo’ sample (thin line). The error bars are indicated at our selected cut  $u_{\min} \leq 0.661$  ( $A_{\max} \geq 1.75$ .)

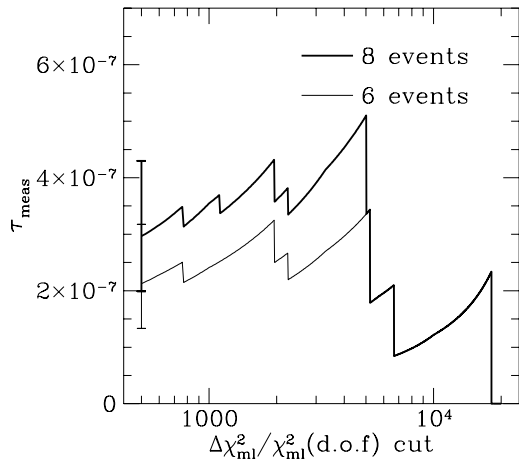


Fig. 15.— The measured microlensing optical depth is plotted as a function of the  $\Delta\chi^2/(\chi_{ml}^2/N_{\text{dof}})$  cut for the 8 event sample (thick line) and the 6 event ‘halo’ sample (thin line). The error bars are indicated at our selected cut  $\Delta\chi^2/(\chi_{ml}^2/N_{\text{dof}}) \geq 500$ .

#### 6.4. Microlensing Rate

The event rate  $\Gamma$  is more model-dependent than the optical depth  $\tau$ , since it depends on the event timescales via the mass function of Machos and their velocity distribution, but the uncertainties on  $\Gamma$  are given purely by Poisson statistics and thus can give very robust limits once the halo model is specified.

The number of observed events is given by Poisson statistics with a mean of

$$N_{\text{exp}} = E \int_0^\infty \frac{d\Gamma}{dt} \mathcal{E}(\hat{t}) d\hat{t} \quad (7)$$

where  $E = 1.82 \times 10^7$  star yr is our total ‘exposure’. As in A96, we have compared our results with the commonly used model of the dark halo (hereafter model S)

$$\rho_H(r) = \rho_0 \frac{R_0^2 + a^2}{r^2 + a^2} \quad (8)$$

where  $\rho_H$  is the halo density,  $\rho_0 = 0.0079 M_\odot \text{ pc}^{-3}$  is the local dark matter density,  $r$  is Galactocentric radius,  $R_0 = 8.5 \text{ kpc}$  is the Galactocentric radius of the Sun, and  $a = 5 \text{ kpc}$  is the halo core radius. We assume a Maxwellian distribution of Macho velocities with an 1-D rms velocity of  $155 \text{ km/s}$ , and (initially) assume a delta-function Macho mass function of arbitrary mass  $m$ . The resulting microlensing rate  $d\Gamma/d\hat{t}$  is given by equation (A2) of A96, and the total rate is  $\Gamma = 1.6 \times 10^{-6} (m/M_\odot)^{-0.5}$  events/star/yr. Thus if our efficiency were 100%, we would expect about  $30 (m/M_\odot)^{-0.5}$  events in the present data set; note that this implies over 1000 events if the halo is made of Jupiters, but only 10 (of longer duration) if it were made of  $10 M_\odot$  black holes; thus, although the optical depth is independent of Macho mass, in a real microlensing experiment the limits on the Macho content of the halo will be strongly dependent on the Macho mass.

It is convenient to define  $\tilde{N}(m)$  to be the number of expected events for an all-Macho halo and unique Macho mass  $m$ ; this function is shown in the upper panel of Figure 16. It is roughly 1.8 times higher than the corresponding curve in A96, due to the doubling in the exposure and the slightly reduced efficiency for the new selection cuts. As before, there are two competing effects; for Macho masses  $\gtrsim 0.01 M_\odot$ , most events have timescales  $\hat{t} \gtrsim 10$  days where our efficiency is quite good, but the event rate is falling  $\propto m^{-0.5}$ . For small masses  $m \lesssim 10^{-3} M_\odot$ , the theoretical event rate is very high but most events are

shorter than  $\hat{t} \sim 3$  days where our efficiency is very low. The product of these two effects causes the peak in  $\tilde{N}(m) \approx 45$  at  $m \sim 10^{-3} M_\odot$ .

Assuming that we have detected not more than 8 microlensing events passing our selection cuts, Poisson statistics exclude at 95% confidence level any model which predicts a mean number of events  $N_{\text{exp}} > 14.5$ ; i.e. we may obtain an upper limit on the fraction of the halo made of Machos of mass  $m$ ,  $f_{\text{lim}}(m) = 14.5/\tilde{N}(m)$ ; this is shown in the lower panel of Figure 16. This limit also applies to arbitrary mass functions within an appropriate interval; if we define  $\psi(m)dm$  to be the fraction of halo density comprised of Machos in the mass interval  $[m, m + dm]$ ; then we have

$$N_{\text{exp}} = \int_0^\infty \psi(m) \tilde{N}(m) dm; \quad (9)$$

thus as pointed out by Griest (1991) and A96, if we set a limit  $f < f_0$  for some constant  $f_0$  for a  $\delta$ -function Macho mass function over some mass interval  $m_1 < m < m_2$ , we also limit the total halo fraction contained within the same interval for any mass function, i.e.  $\int_{m_1}^{m_2} \psi(m) dm < f_0$ ; thus if we draw a line at  $f_0 = 0.5$ , we see from Figure 16 that Machos from  $2 \times 10^{-4}$  to  $0.04 M_\odot$  contribute less than 50% of our standard halo. (We derive a stronger limit below using the event timescales).

We can usefully constrain the total mass of Machos interior to 50 kpc. The above model halo has a mass of  $4.1 \times 10^{11} M_\odot$  within 50 kpc. Thus, the limit on the Macho fraction may be expressed as a limit on the total mass of Machos interior to 50 kpc,  $M_{\text{lim}}(m) = 4.1 \times 10^{11} M_\odot (14.5/\tilde{N}(m))$ . This latter formulation is very useful, because A96 showed that the limits on the Macho *fraction* are quite sensitive to the choice of halo model, but the limits on the *total mass* of Machos within 50 kpc are much less sensitive.

#### 6.5. Limits on Low-Mass Machos

The above analysis utilized only the observed number of events  $N_{\text{obs}}$ . However, there is additional information available in the set of event timescales  $\{\hat{t}_i\}$ . For the halo of equation 8 the expected timescale of microlensing events depends on the mass of the lens as  $\langle \hat{t} \rangle \approx 140 \sqrt{m/M_\odot} \text{ days}$  (Griest 1991). The fact that all 8 of our candidate events have  $\hat{t} \geq 34$  days means that they are unlikely to result from low-mass Machos with  $m \lesssim 0.01 M_\odot$ ; thus, we can obtain considerably stronger limits on such objects by using this

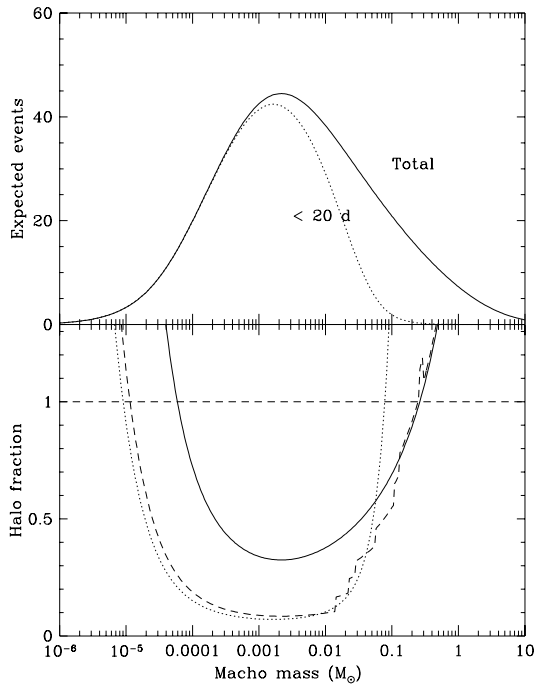


Fig. 16.— Upper panel: expected events for halo model S, for an all-Macho halo with delta-function Macho mass function. The solid line shows the expected total number, the dotted line shows expected number of events with  $\hat{t} < 20$  days. Lower panel: Upper limits on Macho fraction of halo model S. Regions above the curves are excluded at 95% CL. The solid line is derived from 8 observed events, the dotted line from 0 observed events with  $\hat{t} < 20$  days, and the short-dash line from the ‘80% interval’ analysis of §6.5.

information.

We have approached this in two complementary ways: firstly, we can simply note that we have no candidate event with  $\hat{t} < 20$  days (where 20 days is an arbitrary cut conservatively smaller than 34 days); so we can define  $N_{<20}$  to be the expected number of events shorter than 20 days, and exclude at 95% CL any halo model which predicts  $N_{<20} > 3.0$ . This limit is shown as the dotted line in Figure 16; for low-mass Machos it is much more restrictive than the limit in §6.4, since for Macho masses  $< 0.01 M_\odot$  nearly all the events are predicted to have  $\hat{t} < 20$  days, so  $N_{<20} \approx N_{\text{exp}}$ , and the resulting limit on Machos becomes stronger by a factor of  $3.0/14.5 \approx 0.2$ .

While the above approach is very simple, it is subjective, since our choice of the 20-day cut is made *a posteriori*. We have therefore added an alternative approach in which the timescale cuts are defined objectively for each Macho mass using the theoretical distributions. In detail, for each Macho mass, we evaluate the cumulative distribution of expected timescales,

$$N(\hat{t}; m) = E \int_0^{\hat{t}} \frac{dN}{dt}(m) \mathcal{E}(t) dt \quad (10)$$

$$G(\hat{t}; m) = N(\hat{t}; m)/N(\infty; m) \quad (11)$$

i.e.  $G(\hat{t}; m)$  is the average fraction of observed events shorter than  $\hat{t}$  for mass  $m$ . We then compute  $t_1(m)$ ,  $t_2(m)$  such that  $G(t_1; m) = 0.1$ ,  $G(t_2; m) = 0.9$ ; i.e. an interval such that for Macho mass  $m$ , 80% of detected events would have  $t_1 < \hat{t} < t_2$ . Then we count the observed number of events in this timescale interval, which we call  $N_{80}(m)$ , and compute the corresponding Poisson upper limit  $L_{80}(m)$ . This gives a limit on the halo fraction  $f_{\text{lim},80}(m) = L_{80}(m)/0.8\tilde{N}(m)$ , and we repeat this procedure for each value of  $m$ .

For example, given a Macho mass of  $m = 0.1 M_\odot$ , we find that  $t_1 = 20$  days and  $t_2 = 79$  days. We have  $N_{80}(m) = 4$  observed events in this interval, so  $L_{80}(m) = 9.2$  using Poisson statistics. We would expect  $0.8\tilde{N}(0.1 M_\odot) = 16.6$  events in this interval. Thus  $f_{\text{lim},80}(0.1 M_\odot) = 0.55$ .

This limit is shown as the dashed line in Figure 16; the ‘steps’ in the curve occur as events move in and out of the 80% timescale window. We see that this limit is quite similar to the limit derived from  $N_{<20} < 3$  for low masses, and approaches the limit from  $N_{\text{exp}} < 14.5$  for high masses, as expected since our observed timescales are most consistent with high Macho masses  $\gtrsim 0.1 M_\odot$ . The disadvantage to

this approach is that the argument of A96 extending the limits to a continuous mass function is no longer valid, since the “observed” number of events is now a function of the assumed  $m$ . However, this analysis is useful in that it confirms the short-timescale limit from  $N_{<20} < 3$  in an objective way.

We conclude that Machos in the mass interval  $8 \times 10^{-5} - 0.03 M_{\odot}$  contribute less than 20% of the ‘standard’ halo; we extend this to other halo models in § 6.7. In a companion paper (Alcock *et al.* 1996d), we apply a complementary search for very short events ( $0.1 \text{ day} < \hat{t} < 3 \text{ days}$ ) to the current data set; after applying suitable selection criteria, we find no candidates, and thus we extend these limits to lower masses  $\sim 3 \times 10^{-7} M_{\odot}$ .

### 6.6. Likelihood Analysis and Lens Masses

In the above section, we have presented upper limits on low-mass Machos which are valid regardless of the cause of our detected events. However, given that we have a substantial number of events, and the optical depth is a significant fraction of that expected from an all-Macho halo, we need to assess the implications if our observed candidates do result from microlensing by halo objects. Unlike the previous limits on Machos, the conclusions of the next 2 sub-sections depend on the assumption that all 6 or 8 events are due to microlensing by objects in the halo. As discussed in § 6.9, the expected microlensing contribution from all non-halo populations is about 1 event.

For simplicity, we perform likelihood analyses based upon the 6 and 8 event samples similar to those done in A96. A more detailed analysis that includes in the likelihood function models for the density and velocity distribution of background lenses is in progress and will be published elsewhere. As discussed in Section 3.4, the 6 event sample is a reasonable choice for a “halo only” subsample.

Since the timescale of a lensing event is proportional to  $\sqrt{m}$ , we may use the observed timescales to estimate the lens masses, using a maximum-likelihood method as in A96. We use a 2-parameter model where a fraction  $f$  of the dark halo is made of Machos with a unique mass  $m$  (the remaining  $1 - f$  of the halo is assumed to be in Machos outside our mass range, or particle dark matter). The likelihood of finding a set of  $N_{\text{obs}}$  detected events with timescales

$\hat{t}_i, i = 1, \dots, N_{\text{obs}}$  is given by

$$L(m, f) = \exp(-f\tilde{N}(m)) \prod_{i=1}^{N_{\text{obs}}} \left( f E \mathcal{E}(\hat{t}_i) \frac{d\Gamma}{d\hat{t}}(\hat{t}_i; m) \right), \quad (12)$$

where  $d\Gamma/d\hat{t}$  is the theoretical rate of microlensing derived from a halo model. The results are dependent on the model so in § 6.7 we explore a range of possible halos. For model S, the resulting likelihood contours, assuming a delta-function mass function, are shown in Figure 17; the probabilities are computed using a Bayesian method with a prior uniform in  $f$  and  $\log m$ . We show plots for both our 6 event sample and our 8 event sample. We think the the 6 event sample gives the more reliable estimate for halo lenses, but we also show the results of the 8 event sample to span the range of possibilities. The peak of the likelihood contours gives the most probable mass and halo fraction for this model and for the 6 event sample we find  $m_{2D} = 0.41 M_{\odot}$ , and  $f_{2D} = 0.51$ .

We calculate the one-dimensional likelihood function by integrating over the other parameter and find (for the 6 event sample) a most likely Macho mass  $m_{ML} = 0.46^{+0.30}_{-0.17} M_{\odot}$ , and most likely halo fraction  $f_{ML} = 0.50^{+0.30}_{-0.20}$ . The errors given are 68% CL. The values for the 8 event sample are also given in Table 9. It is important to note the large extent of the contours in Figure 17. This is mostly due to the small number of events. For model S, the 95% CL contour includes halo fractions from 17% to 100%, and Machos masses from 0.12 to  $1.2 M_{\odot}$ .

The most probable mass and halo fraction are both larger than our results from year-1, which were  $m = 0.06 M_{\odot}$  and  $f = 0.2$ , though there is a reasonable degree of overlap of the contours. The year-1 90% CL contour is shown as the light line in Figure 17. The most probable value of each analysis lies outside the 90% CL contour of the other analysis. This is due to the fact that events 2 & 3 from A96 (with  $\hat{t} = 20$  and 28 days) have dropped out of our new sample, and all of the new events are longer than all the A96 events. This probably reflects small-number statistics, and the improved efficiency for longer-timescale events with the 2-year data.

A notable feature with the new results is that a delta-function mass of  $0.1 M_{\odot}$  is marginally excluded. This would exclude brown dwarfs as the dominant lens population, since a realistic brown-dwarf population cannot include a significant fraction of objects above  $0.1 M_{\odot}$  due to star-count data (e.g. Bahcall



*et al.* 1994; Hu *et al.* 1994), while it should include smaller masses which would worsen the likelihood.

Given the importance of such a conclusion, we next ask how dependent are the results obtained here to the halo model and to delta-function mass distribution assumption.

### 6.7. Power-Law Halo Models

Although the halo model of eq. 8 is a widely used baseline for comparison, there are few tracers of the mass distribution in the outer Galaxy and thus a considerable uncertainty in the real halo parameters. To check the model dependence of our results, we have repeated our analysis for a wide range of ‘power-law’ halo models (Evans 1993). For simplicity, we have used the same set of models as in Table 2 of A96, and they are described in detail there. The set of models used span an extreme set of probable halo masses, so any conclusions which hold for this set of models are probably quite robust. Briefly, the models consist of extremes which match the measured Milky Way rotation curve at  $r_0$  and  $2r_0$ , and which have a range of disk masses. They do not include the Galactic bulge or bar. Model A is a power-law equivalent of model S; model B has a very massive halo with rising rotation curve; model C has a light halo with a falling rotation curve, and model D has the same rotation curve as model A but a halo flattened to about E6. Models E, F and G have more massive disks and less massive halos, with model E being an extreme ‘maximal disk/minimal halo’ model and models F, G being more realistic ‘heavy disk’ models.

The expected number of events  $N_{\text{exp}}$  for each model is shown in Figure 18, and the resulting upper limits on halo Macho fraction are shown in Figure 19. The expected number of events with  $\hat{t} < 20$  days  $N_{<20}$  is shown in Figure 21; the corresponding limits on halo fraction  $f_{\text{lim}} = 3/N_{<20}$  are shown in Figure 22, and the limits on total mass of Machos interior to 50 kpc are shown in Figure 23. As in § 6.5, the latter limit is much stronger for small Macho masses. Except for the unlikely model E, we find that for all the models, Machos between  $\sim 2 \times 10^{-5} M_{\odot}$  and  $0.01 M_{\odot}$  contribute less than  $10^{11} M_{\odot}$  to the halo mass within 50 kpc.

The maximum likelihood estimates of Macho mass  $m$ , halo fraction  $f$ , and total mass of Machos for the 8 models are shown in Figure 24 and listed in Table 9. As in A96, we find that both the limits

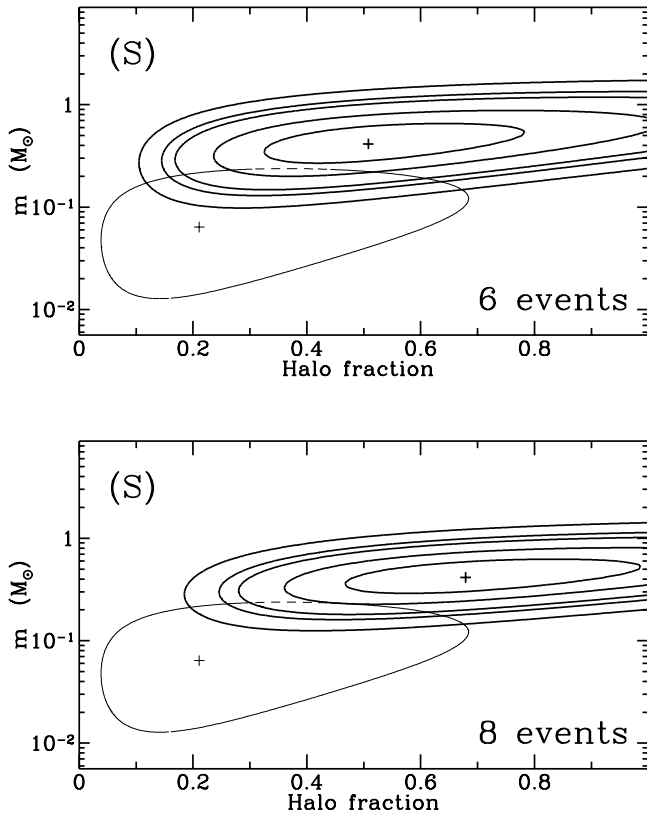


Fig. 17.— Likelihood contours of Macho mass  $m$  and halo Macho fraction  $f$  for a delta-function mass distribution, for halo model S. The most likely value is indicated with a +, and the contours enclose total probabilities of 34%, 68%, 90%, 95%, 99%, using a Bayesian method as described in § 6.6. The light line shows the 90% contour from A96.

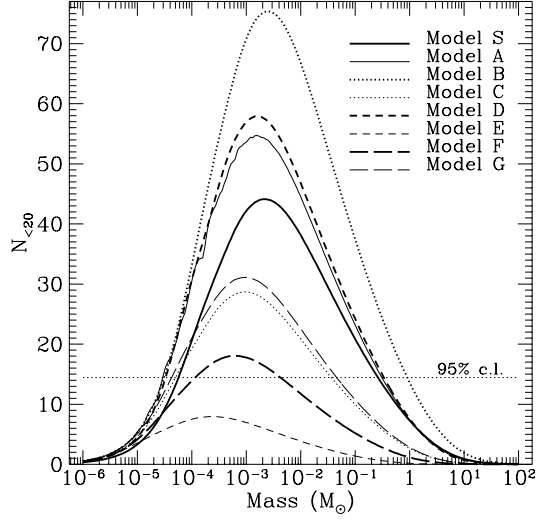


Fig. 18.— Expected number of events for the 8 halo models S, A-G, with all-Macho halo and delta-function mass function. The 95% CL upper limit is for the 8 event sample.

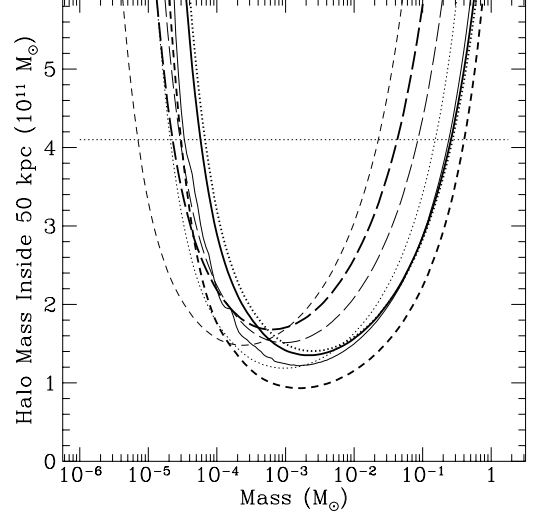


Fig. 20.— Upper limits (95% CL) on the total mass of Machos within 50 kpc for halo models S, A-G, based upon 8 observed events. Line coding as Figure 18.

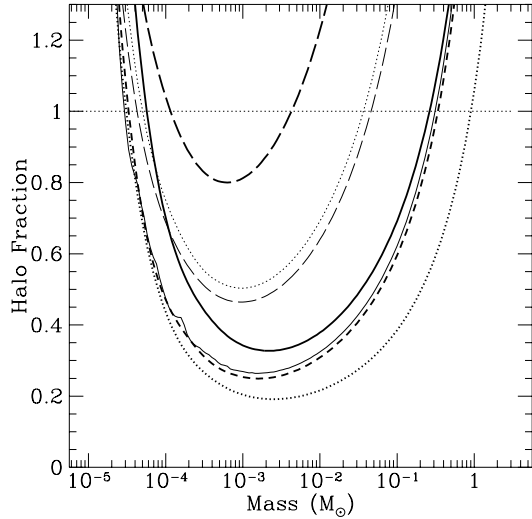


Fig. 19.— Upper limits (95% CL) on the fraction of the halo made of Machos for the 8 halo models S, A-G based upon 8 observed events. Line coding as Figure 18.

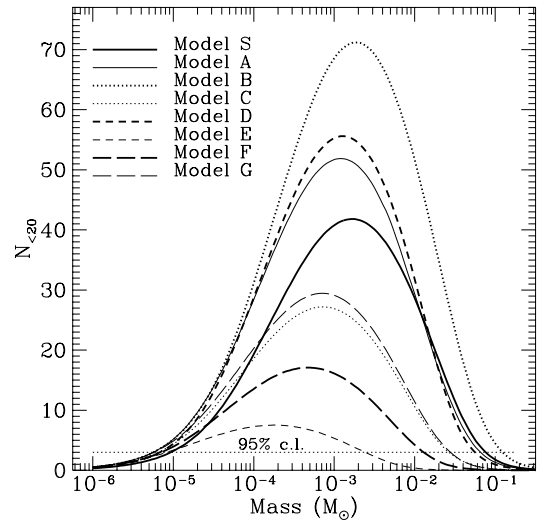


Fig. 21.— Expected number of events with  $\hat{t} < 20$  days for halo models S, A-G, with delta-function Macho mass function. Line coding as Figure 18.

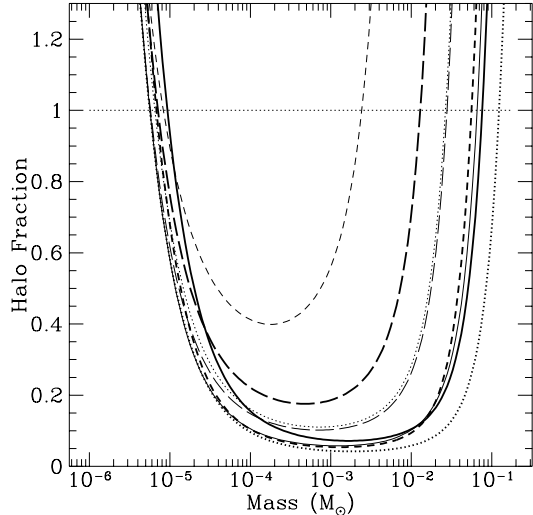


Fig. 22.— Upper limits (95% CL) on the fraction of the halo made of Machos for models S, A-G, based on no observed events with  $\hat{t} < 20$  days. Line coding as Figure 18.

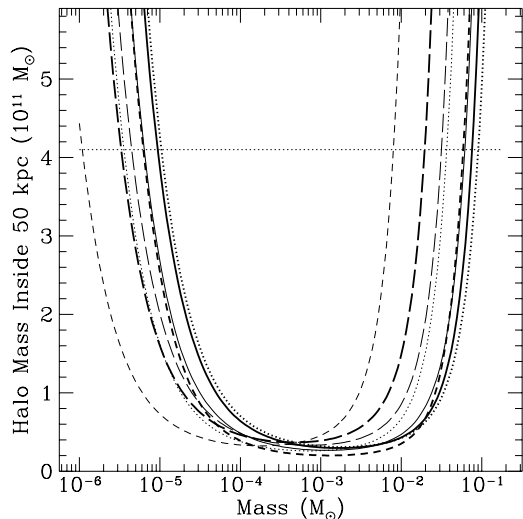


Fig. 23.— Upper limits (95% CL) on the the total mass of Machos within 50 kpc for models S,A-G, based on no observed events with  $\hat{t} < 20$  days. Line coding as Figure 18.

$f_{\text{lim}}(m)$  and the most probable halo fraction  $f_{ML}$  and Macho mass  $m_{ML}$  are quite model-dependent, with most probable halo fractions ranging from 30% to 100%, and most probable Macho masses ranging from less than  $0.1 M_{\odot}$  to almost  $0.6 M_{\odot}$  (in the 6 event sample which is the best to use for this purpose). Thus the uncertainty introduced due to the halo model is almost as great as the Poisson errors due to the small number statistics. However, when we scale the results by the total halo mass within 50 kpc, giving  $M_{\text{lim}}(m) = f_{\text{lim}}(m)M_H(50 \text{ kpc})$  and  $M_{ML}(m) = f_{ML}M_H(50 \text{ kpc})$ , the results are rather insensitive to changes in the halo model. For limits this is shown in Figure 23. The most probable halo masses are shown in column 6 of Table 9. Thus for the 6 event data set, we find a most probable halo mass in Machos within 50 kpc of  $2_{-0.7}^{+1.2} \times 10^{11} M_{\odot}$  almost independent of the halo model. As discussed in A96, this model independence is not too surprising, since our experiment is not sensitive to the total halo mass, but only to the mass in Machos. It is worth noting that this is several times the mass of all known stellar components of the Milky Way. If the bulk of the lenses are located in the halo, then they represent the dominant identified component of our Galaxy, and a major portion of the dark matter.

The model independence of the total halo mass in Machos contrasts with the model dependence of the most probable lens mass. One notes that that the lighter halo models such as C, E, F, G have a smaller implied Macho mass  $m_{ML}$ . This arises because lighter halos have a smaller velocity dispersion and thus we expect longer timescale microlensing events for a given mass, i.e. smaller implied masses for a given observed timescale. Also, the lighter halos tend to have larger core radii, thus the lenses are on average more distant, which also goes in the direction of lengthening the events. Since  $\hat{t} \propto \sqrt{m}$ , i.e.  $m \propto \hat{t}^2$ , this effect can be quite substantial. The 95% CL contours of models C, E, F, and G overlap considerably the brown dwarf mass range  $m < 0.1 M_{\odot}$ . We note that the implications for the formation of the halo could be dramatically different in this case. We also note that rotation of the halo could lower the expected lens mass range, but these results will be presented elsewhere.

Also shown in column 7 of Table 9 are the optical depths calculated from the halo fraction for each model. These values and their confidence intervals are simple to interpret statistically, since each model

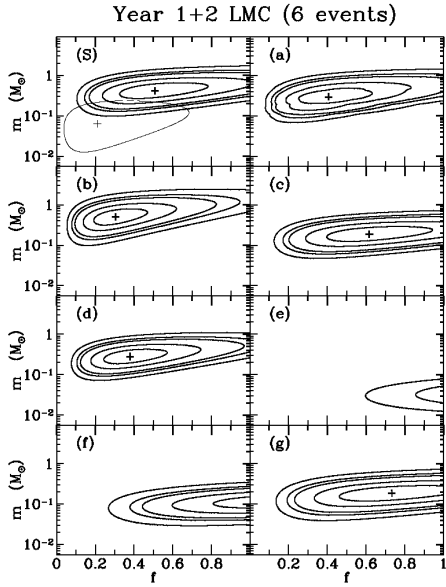


Fig. 24.— (a) Likelihood contours for Macho mass  $m$  and halo fraction  $f$  for halo models S, A-G, from the 6-event sample. The + shows the maximum likelihood estimate, and the contours enclose regions of 34%, 68%, 90%, 95% and 99% probability. For model S, the 90% contour for year 1 LMC data (A96) is also shown. The models are described in A96.

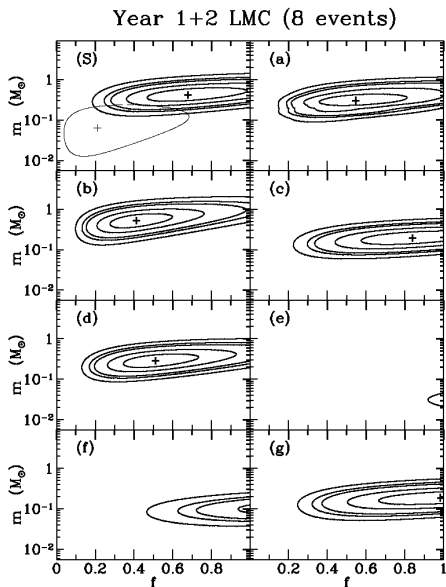


Figure 24 (b) – As (a) for the 8-event sample.

provides a distribution of event durations. Thus the subtleties discussed in Section 6.1 are absent. We note that these values are quite independent of the halo model, and are very close to the values we obtained in our direct estimates.

## 6.8. Other Mass distributions

Delta function mass distributions are simple to analyze and easy to understand, but *a priori* are quite unlikely, so we explored a range of other options. We repeated our likelihood analysis using a power-law mass distribution,

$$\psi(m) = Am^\alpha \quad (m_{min} < m < m_{max}) \quad (13)$$

$$= 0 \quad (\text{otherwise})$$

with the normalization constant  $A$  determined from  $\int_{m_{min}}^{m_{max}} \psi(m) dm = f$ , where  $\psi(m)dm$  is the mass fraction between  $m$  and  $m + dm$ . Here we take the slope  $\alpha$ , cut-off mass  $m_{min}$  and halo fraction  $f$  as the free parameters in the likelihood function. We fixed the maximum mass at  $12 M_\odot$ , since our results did not much depend on its value. For the 6 event sample we found that the slope became as negative as possible, and that the minimum mass approached the delta-function mass model most probable mass. Thus the most probable power-law is the one which most closely approximates the delta-function mass distribution used earlier! This can be understood by examining the predicted distribution of events. As shown in Figure 25a, the most likely delta function mass model ( $m_{2D} = 0.41$ ,  $f_{2D} = 0.51$ ) predicts a distribution of durations that matches well the observed distribution. A non-delta mass distribution would necessarily have a more spread out duration distribution, which would be a worse fit to this rather narrow observed event set. However, we note that the difference in likelihood between the delta-function model and the most likely power-law model with  $\alpha$  fixed at  $-2$  (with its most likely  $m_{min} = 0.23$  and  $f = 0.54$ ) is only 16%. Thus, our data are not really capable of distinguishing these two cases, as can be seen from the dashed curve in Figure 25a.

For the 8 event sample, the most likely distribution is a non-delta function distribution with the very steep slope  $\alpha = -3.9$ ,  $m_{min} = 0.30 M_\odot$ , and  $f = 0.66$ . This model is favored over the most likely delta-function model ( $m_{2D} = 0.40 M_\odot$ ,  $f_{2D} = 0.65$ ) by only 2% in likelihood. A single event of longer duration makes the more spread out duration distribution a slightly better fit to this wider observed event set, as can be seen in Figure 25b. The 6 and 8 event sample sets have the same best fit delta-function mass because the two samples have approximately the same mean  $\hat{t}$ . The two samples do not have the same most likely fraction. In fact, by setting the derivative with

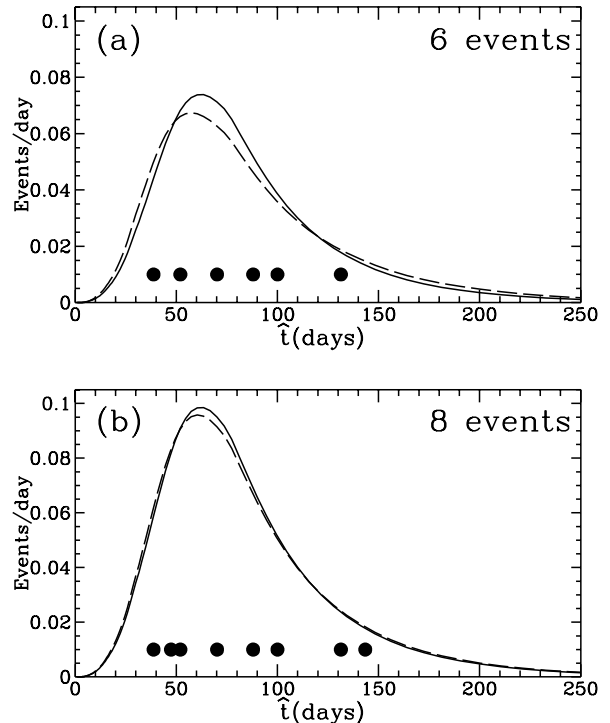


Fig. 25.— Distribution of durations ( $\hat{t}$ ) for maximum likelihood models. In part (a) (6 event sample), the solid line is for the best fit model with a delta-function mass ( $m_{2D} = 0.41$ ,  $f_{2D} = 0.51$ ), while the dashed line is for the best power law mass distribution with slope fixed at  $\alpha = -2$  ( $m_{min} = 0.23$ ,  $f = 0.54$ ). The large dots indicate the observed  $\hat{t}$ 's. The delta-function model has a larger likelihood. In part (b) (8 event sample), the solid line is for the best fit power law mass distribution ( $\alpha = -3.9$ ,  $m_{min} = 0.30$ ,  $f = 0.66$ ), which has a slightly higher likelihood than the dashed line best fit delta-function model ( $m_{2D} = 0.40$ ,  $f_{2D} = 0.65$ ).

respect to  $f$  of Equation (12) equal to zero, we can show that the most likely  $f$  for given  $m_{min}$  and  $\alpha$  is that  $f$  which makes the expected number of events equal to the observed number of events. It is for this reason that the plots on Figures 25a and b normalize to 6 and 8 expected events respectively.

### 6.9. Microlensing by Non-Halo Populations

The implications of the above sections are very striking. We clearly need to assess the significance of the difference between our estimate of the optical depth, and the optical depth due to known populations of objects. In particular, could all of our candidate microlensing events arise from microlensing by known populations of low-mass stars? As noted by Wu (1994), Sahu (1994), De Rujula *et al.* (1995) and A96, low-mass stars in the Galaxy and LMC may give rise to microlensing events. These authors find that the optical depth from known stars is only  $\lesssim 10\%$  of that from an all-Macho halo, but is not negligible. This may be understood qualitatively since the microlensing ‘tube’ is wider in the middle and narrow near the Sun and LMC (Griest 1991).

For obtaining confidence intervals, it is better to work with microlensing rates rather than optical depth; thus, we have repeated the estimates of stellar lensing rates of A96, using the same model parameters for the thin and thick disks, the spheroid and the LMC disk, assuming a Scalo Present Day Mass Function (PDMF) for all populations, and simply updating the efficiency curves and the total exposure for our 2-year dataset. Two values are given in Table 10 for the LMC disk, first at the center and secondly averaged over our fields assuming a 1.6 kpc scale length. The values for halo S are also shown for comparison, though a Scalo PDMF for the halo is implausible.

The results are shown in Table 10; the expected number of events is  $\approx 2\times$  higher than in A96. We see that in our present sample, we would expect to observe 0.71 events from stars in the LMC disk, 0.29 from the Milky Way thin disk, and only 0.075 from the thick disk and 0.066 from the spheroid. This gives a total ‘background’ of 1.14 expected events from all known stellar populations and a total background optical depth of  $0.54 \times 10^{-7}$ .

For a Poisson distribution with a mean of 1.14, the probabilities to observe  $N_{obs} \geq 3, 4, 5, 6, 7$  are 10.7%, 2.9%, 0.6%, 0.11%, 0.02% respectively. Thus we see that if only 3 of our events are genuine mi-

cro-lensing, the evidence for an excess is modest, whereas if  $\geq 4$  of our events are microlensing there is very strong evidence for an excess over stellar lensing alone.

Since we have 4 ‘excellent’ microlensing candidates, it might be tempting to adopt the ‘null hypothesis’ that these 4 result from lensing by stars (which is only improbable at the 3% level); the other candidates are not microlensing (e.g. they are variable stars), and then there is only weak evidence for Machos in the halo. However, as noted in Section 3.2 there is a flaw in this argument, in that the distribution of microlensing magnifications is given *a priori*, and the ‘excellent’ microlensing candidates are preferentially the high-magnification ones. Thus, we should expect to find a mixture of ‘excellent’, ‘good’ and ‘moderate’ candidates, and it is unlikely that all events would be ‘excellent’ (whatever the exact definition).

We can use this argument in two ways: firstly, we can add an additional selection cut  $A_{max} > 2.5$ , which leaves 4 microlensing candidates (1,4,5,7) including 3 ‘excellent’ ones; this cut reduces the detection efficiency (normalized to the event rate with  $A_{max} > 1.34$ ) by a factor of 0.71, so the expected number of stellar lensing events is reduced to 0.81, and the probability of  $\geq 4$  such events is then only 0.9%.

Secondly, we can use the results in Table 5 for the impact parameter distribution; if we assume that events 1, 4, 5 are microlensing, the observed impact parameter distribution is improbable at the 10% level unless at least one other event is also microlensing. Since the binary event does not count in this table but is almost certainly microlensing, this suggests that we have observed at least 5 microlensing events in total, which is improbable at the 0.6% level from our model of the stellar populations.

Thus, we have seen that there appears to be a significant excess of lensing events above the expectation from stellar lensing; this is true regardless of whether we have observed 4, 5, 6 or 7 real lensing events, so does not depend sensitively on the lower-quality microlensing candidates.

The main caveat here is that there is some uncertainty in the stellar lensing predictions. For the thick disk and spheroid, this is not important since their contributions are very small. For the thin disk, we have assumed a local column density of  $50 M_{\odot} \text{pc}^{-2}$  for the lens population. Dynamical constraints limit

the total local column density to  $\lesssim 80 M_{\odot} \text{pc}^{-2}$ , and part of this is in bright stars which will not give detectable lensing, and part in gas which does not lens. Thus the optical depth from the thin disk cannot be much higher than our model value.

For lensing by LMC stars, the uncertainties are substantially larger. The optical depth is proportional to  $\Sigma h \sec^2 i$ , and the event rate is proportional to  $\Sigma \sqrt{h} \sec i / \sigma$  where  $\Sigma$  is the face-on column density,  $h$  is the scale height and  $\sigma$  is the transverse velocity dispersion.

In Table 10 assume  $\Sigma_0 = 363 M_{\odot} \text{pc}^{-2}$ ,  $h = 250 \text{pc}$ ,  $i = 30^\circ$  and  $\sigma = 25 \text{km/s}$  for the LMC, so the important question is how much we could increase these numbers without conflicting with dynamical observations. For the above  $\Sigma_0$  and an exponential scale length of 1.6 kpc, the LMC rotation curve peaks at 77 km/s, close to the observed value. Thus, it is unlikely that  $\Sigma_0$  is much higher than our estimate, but the constraints on  $h$  are considerably weaker. However, Gould (1995a) has proved a very general relation  $\tau = 2 \langle v^2 \rangle \sec^2 i / c^2$  between the optical depth from a self-gravitating disk and the observed line-of-sight velocity dispersion. For old populations in the LMC, the observed  $\langle v^2 \rangle \lesssim 30 \text{km/s}$ ; this gives an optical depth of  $\lesssim 2.6 \times 10^{-8}$  from LMC self-lensing, which is somewhat smaller than our estimate.

If we assume conservatively that the expected number of events from LMC stars could be twice the above estimate i.e. 1.42, this gives a total of 1.85 expected stellar lensing events in our data (this would seem to require a large velocity dispersion  $\gtrsim 60 \text{km/s}$  for the old LMC population). The probability of  $N_{\text{obs}} \geq 3, 4, 5, 6, 7$  is then 28%, 11%, 4%, 1%, 0.3% respectively, so if 5 or more events are microlensing there is still a significant excess, but if 4 or fewer events are microlensing it is only slightly improbable.

Thus, it is not impossible to explain our results by stellar lensing alone, but we have to stretch in several directions simultaneously; we have to push the observed number down to 4 microlensing events, adopt a non-standard LMC model to get the expected number up close to 2, and bridge the remaining gap with a statistical fluctuation.

## 7. Summary and Discussion

If the observed 8 candidate events are microlensing, the implied optical depth is considerably higher than expected from known stars alone. In comparison with

our A96 results, the implied event rate is similar ( $\sim 7$  events in 2.1 years compared with 3 events in 1.1 years), but the longer timescales for the new sample lead to considerably higher optical depth and halo mass estimates. While the uncertainties are still large, the observed lensing rate is a significant fraction of that predicted in the standard model of the Galactic dark matter halo.

Using a likelihood analysis to extract information from the distribution of event timescales shows a significant model dependence in the derived halo fraction and the individual lens masses. The total inferred mass in lenses within 50 kpc is quite insensitive to the model parameters, however, as is the optical depth found via likelihood analysis. These optical depth estimates and the corresponding confidence intervals are quite close to our directly estimated optical depth value, and are statistically simple to interpret.

The experiment's sensitivity to long duration events will improve over time, and the event tally will presumably increase as well. Prospects for refining our knowledge of the optical depth are therefore promising.

One natural explanation of the results presented here is that a substantial fraction of the Galactic dark halo may be made of compact objects. We now speculate as to what astrophysical objects might be responsible for the observed signal. The fact that the observed events have relatively long timescales suggests that (for standard halo models) the lenses have masses above  $\sim 0.1 M_{\odot}$ , with a most probable mass  $\sim 0.5 M_{\odot}$ . If so, they cannot be ordinary hydrogen-burning stars since there are strong direct limits on such objects from counts of faint red stars (e.g. Bahcall *et al.* 1994; Hu *et al.* 1994; Flynn, Gould & Bahcall 1996); thus stellar remnants such as white dwarfs appear to be the most obvious possibility. However, our exploration of halo models also showed that for 'minimal' halos, the timescales may still be consistent with substellar Machos just below  $0.1 M_{\odot}$ . Also, models with a substantial degree of halo rotation may lead to smaller mass estimates, since the rotation could reduce the transverse component of the Macho velocities. Thus, brown dwarfs cannot be ruled out as yet, but they would require both a non-standard halo model and a mass function concentrated close to the H-burning limit.

There are some theoretical difficulties with the white-dwarf hypothesis (Carr 1994 & refs. therein); firstly, the initial mass function must be fairly sharply

peaked between  $\sim 2 - 6 M_{\odot}$  to avoid overproducing either low-mass stars (which survive to the present) or high-mass stars (which explode as type-II SNe and overproduce metals). The second difficulty is that the high luminosity of the B and A stars which are the WD precursors may exceed the observed faint galaxy counts (Charlot & Silk 1995), though this may possibly be evaded by dust.

Primordial nucleosynthesis can also provide interesting constraints on baryonic dark matter. The primordial deuterium abundance is, in principle, a sensitive indicator of the total baryonic density of the universe. The observational situation is unclear at present with some measurements indicating a low deuterium abundance (Tytler, Fan, & Burles 1996; Burles & Tytler 1996) and other observations indicating a high abundance (Songaila *et al.* 1994; Carswell *et al.* 1994; Rugers & Hogan 1996). If the low abundance measurements indicate the actual primordial deuterium abundance, then a substantial amount of baryonic dark matter must exist. On the other hand, if the primordial deuterium abundance is low, then there is probably not enough baryonic dark matter to explain galactic rotation curves. Nevertheless, as Rugers & Hogan (1996) point out, even if the primordial deuterium abundance is high, primordial nucleosynthesis predicts that the total baryonic mass in our Galaxy is  $\sim 2.4 \times 10^{11} M_{\odot}$  (for  $H_0 = 70 \text{ km/sMpc}^{-1}$ ) which is consistent with a Macho component of the dark halo as the source of the bulk of the microlensing events.

On the positive side, white dwarfs (along with neutron stars and neutrinos) are the only dark matter candidates which are known to exist in large numbers. Also, it has recently become clear (e.g. White *et al.* 1993) that the mass of hot gas in rich galaxy clusters greatly exceeds that in stars, and furthermore this gas is relatively metal-rich with an iron abundance  $\sim 0.3$  solar (Mushotzky 1996). This might suggest that most of the baryons have been processed through massive stars, which have since died leaving a population of remnants and metal-rich gas. This scenario has been explored by Fields, Mathews & Schramm (1996), who suggest that it may be natural to have 40-100% of the Galactic dark matter in white dwarfs.

The observational limits on the local density of white dwarfs are a strong function of their age (e.g. Liebert, Dahn & Monet 1988); until recently, for ages  $\gtrsim 12$  Gyr expected for dark-matter white dwarfs, the present limits were an order of magnitude above the

halo density. These limits were mostly derived from plate-based proper motion surveys, and with modern CCD arrays sensitive in the I-band, they could be improved by a large factor. Very recently, a limit from the Hubble Deep Field has been given by Flynn, Gould & Bahcall (1996); they find that white dwarfs with  $M_I < 16$  contribute  $< 100\%$  of the halo density, and those with  $M_I < 15$  contribute  $< 33\%$ .

These limits, while tantalizing, are still not stringent enough to conflict with a large population of old white dwarfs in the halo as an explanation of our microlensing results; but if such a population exists, their local counterparts should be detectable in the fairly near future.

However, it is worth noting that microlensing is sensitive to any compact objects, irrespective of composition, as long as they are smaller than their Einstein radii  $\sim 3$  AU. Thus, more exotic objects such as primordial black holes, strange stars or ‘shadow stars’ are possible, and these would be virtually undetectable by direct searches.

There are a number of prospects for clarifying the origin of our events: firstly, we have now implemented real-time data processing for most of our fields, so we hope that most future events should be detected in real time. Follow-up observations such as frequent high-precision photometry and spectroscopy should help to check that our events are not due to intrinsic stellar variability. For example, our second LMC ‘alert’ event 96-LMC-1 was detected on 1996 February 11 and announced in IAU Circular 6312; follow-up at CTIO shows a good fit to microlensing, with  $A_{\text{max}} = 2.4$  and  $\hat{t} = 90$  days.

Secondly, we can discriminate between microlensing by halo or LMC objects using the spatial distribution of events, as in § 5. Although the current sample does not provide a strong test, enlarging the sample by a factor  $\sim 2 - 3$  should clarify this. Our project will continue until 1999 December, and since late 1994 we have modified our observing strategy to observe more fields less frequently than the current sample. This should increase the detection rate for events with  $\hat{t} \gtrsim 30$  days, and since the additional fields are further from the center of the LMC, it will also provide a better ‘lever arm’ for testing the spatial distribution. Also the EROS and OGLE groups plan to have new telescopes operating in Chile by late 1996, which should increase the detection rate.

Thirdly, it should be possible to improve the pre-



dictions of the microlensing rate from LMC stars by direct observation; for example, radial velocity measurements for a large sample of LMC RR Lyrae stars would provide an important check of the dynamics of the old LMC population. If these show a velocity dispersion  $\lesssim 60$  km/s, it would exclude LMC stars as the main contribution to the observed lensing (Gould 1995a).

Finally, the ideal method for locating the lens population is to get ‘parallax’ measurements by following up the events from a small telescope in Solar orbit (Gould 1994b; Gould 1995b). This measures the velocity of the lens projected to the Solar system, which provides a definitive proof of microlensing, and can discriminate between disk, halo and LMC lenses on an event-by-event basis.

To summarize, we have two main conclusions: firstly, Machos in the mass range  $\sim 10^{-4}$  to  $0.03 M_{\odot}$  do not contribute significantly to the galactic dark matter. Secondly, our results indicate a microlensing optical depth of  $\approx 3 \times 10^{-7}$  or a Macho mass within 50 kpc of  $\approx 2 \times 10^{11} M_{\odot}$ . This provides evidence that Machos with masses in the range  $0.05 - 1 M_{\odot}$  contribute a substantial fraction of the galactic dark halo. Continued observations from this and other projects should clarify this in the next few years.

## Acknowledgments

We are very grateful for the skilled support given our project by the technical staffs at the Mt. Stromlo and CTIO Observatories, and in particular we would like to thank Mr. S. Chan and Mr. G. Thorpe for their invaluable assistance in obtaining the data. We thank the NOAO for making nightly use of the CTIO 0.9 m telescope possible. We thank S. Rhie for contributing to the binary fitting code used for Figure 6. Work performed at LLNL is supported by the DOE under contract W7405-ENG-48. Work performed by the Center for Particle Astrophysics personnel is supported in part by the Office of Science and Technology Centers of NSF under cooperative agreement AST-8809616. Work performed at MSSSO is supported by the Bilateral Science and Technology Program of the Australian Department of Industry, Technology and Regional Development. WJS is supported by a PPARC Advanced Fellowship. KG acknowledges support from DOE Outstanding Junior Investigator, Alfred P. Sloan, and Cottrell awards. CWS thanks the Sloan, Packard and Seaver Foundations for their

generous support.

## Appendix A

We believe that the blending efficiencies shown in Figure 8 are a reasonably accurate estimate of our actual microlensing detection efficiencies,  $\mathcal{E}$ , but it is also worthwhile to establish an absolute upper limit on our detection efficiency. An absolute upper limit on  $\mathcal{E}(\hat{t})$  translates into a firm lower limit on the microlensing optical depth that will be free of systematic errors due to blending effects.

The upper limit efficiency that we will consider will be an ‘‘optical depth’’ efficiency,  $\mathcal{E}_{\tau}(\hat{t})$ , rather than the event detection efficiency described in the previous section. The optical depth,  $\tau$ , is defined to be the probability that a given source star is located within the Einstein radius of any lensing object, or equivalently the probability,  $P(A \geq 1.34)$ , that a lens has magnified the source star by a factor  $\geq 1.34$ . One could also consider the probability that a star is magnified by a factor of more than some threshold  $A_T$ . The optical depth would then be given by  $P(A > A_T)/u_T^2$  where  $u_T$  is related to  $A_T$  by  $A_T = (u_T^2 + 2)/(u_T \sqrt{u_T^2 + 4})$ . For a microlensing experiment which observes many stars for a finite period of time this becomes

$$\tau_{\text{obs}} = \frac{1}{E} \sum_i \frac{T_i(A > A_T)}{u_T^2 \epsilon_i}, \quad (\text{A1})$$

where  $E$  is the total stellar exposure (in star-years) and  $T_i(A > A_T)$  is the amount of time that event  $i$  is magnified by a factor larger than  $A_T$ , and  $\epsilon_i$  is the efficiency for detecting event  $i$ . Equation (A1) is correct assuming unblended stellar images, but now let us consider the effect of blending. In cases when our lightcurves are derived from blends of two or more unresolved stellar images, there are two effects: a) The detection threshold is effectively raised because the lensed star must be magnified by a larger factor to compensate for the fact part of the ‘‘source’’ is not lensed, and b) there is more than one source that can be lensed. Clearly, these two effects tend to cancel. We will show, however, that as long as  $A_T > 1.34$  ( $u_T < 1$ ), the effect of blending will always be to *reduce* the optical depth estimate of equation (A1).

Let’s consider a blended stellar image consisting of  $N$  stars each contributing a fraction,  $f_i$ , of the total flux so that  $\sum f_i = 1$ . We’ll try to estimate

the optical depth using equation (A1), and we will see how the contribution of the image blend to equation (1) compares to the contribution of an unblended source. Each member of the image blend now has a different effective magnification threshold given by  $A_{Ti} - 1 = (A_T - 1)/f_i$ . These effective magnification thresholds can be translated into threshold radii,  $u_{Ti}$  using equation (1). Then, the contribution of all the stars in the blend to the optical depth is just given by the ratio of the sum of the areas of the circles of radius  $u_{Ti}$  for each actual star to the area of the single circle corresponding to the unblended source that was originally assumed. This means that the apparent microlensing optical depth is modified by the multiplicative factor  $\sum u_{Ti}^2/u_T^2$ . This is just the change due to blending of the area on the sky that can have a (blended) magnification  $> A_T$ . Figure 26 shows the blend inefficiency factor,  $u_{Ti}^2/(f_i u_T^2)$ , as a function of  $f_i$  and  $u_T$ . For  $u_T < 1$ , this factor is always  $< 1$ . This means that each blended star will contribute a fraction  $< f_i$  toward the total optical depth as compared to the optical depth in the unblended case. Since  $\sum f_i = 1$ , this implies that the blended stars will contribute less to the optical depth than an unblended star would. Thus, blending can only serve to decrease the observed microlensing optical depth.

There are a few caveats regarding applying this argument to our experiment. First, we do not use equation (A1) to determine our measured optical depth. Instead, we use the  $\hat{t}$  values from unblended microlensing fits which are shown in Table 3 and Figure 3. Inspection of this figure indicates that these fit values do not seriously underestimate the time that the stars are magnified by more than (say) 1.75. Thus, this detail should not affect our conclusion. Another caveat that we must consider is that this argument implicitly assumes that blending does not make events easier to detect. The one case in which blending *does* make an event easier to detect is the case of events with  $\hat{t} > 300$  which are excluded by our timescale cuts. With a blended event, the fit  $\hat{t}$  values from the unblended fits used in our event selection analysis generally underestimate the actual  $\hat{t}$  values, so an event with  $\hat{t} > 300$  days might appear to be an (unblended) event with  $\hat{t} < 300$  days which would pass our cuts.  $\mathcal{E}(\hat{t})$  only enters the optical depth calculation evaluated at the measured  $\hat{t}$  values, so this point has no effect on our optical depth estimate because our longest detected event has  $\hat{t} < 150$  days.

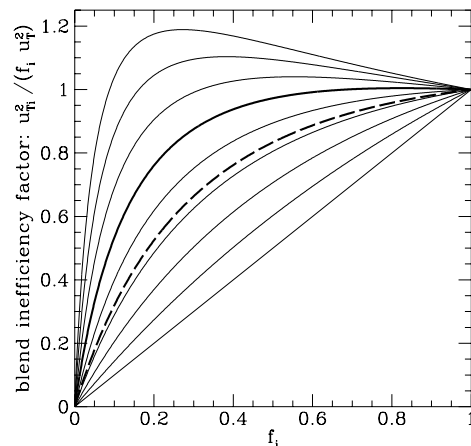


Fig. 26.— The blend inefficiency factor:  $u_{Ti}^2/(f_i u_T^2)$  is plotted as a function of  $f_i$  for  $u_T = 0$  (bottom), 0.2, 0.4, 0.6, 0.661 (dashed), 0.8, 1.0 (thick), 1.2, 1.4 and 1.6 (top). The dashed line corresponds to our event detection threshold of  $A_T = 1.75$ . These curves indicate how much the optical depth efficiency is reduced by blending as a function of  $f_i$  and  $u_T$ . For  $u_T < 1$  blending always *decreases* the optical depth efficiency.

## REFERENCES

- Alard *et al.*, 1995a, ESO Messenger, 80, 31.
- Alard, C., Mao, S. & Guibert, J., 1995, A&A, 300, L17.
- Alcock, C. *et al.*, 1993, Nature, 365, 621
- Alcock, C. *et al.*, 1994, IAU Circ., 6095
- Alcock, C. *et al.*, 1995a, Phys. Rev. Lett., 74, 2867
- Alcock, C. *et al.*, 1995b, ApJ, 445, 133
- Alcock, C. *et al.*, 1995c, ApJ, 454, L125
- Alcock, C. *et al.*, 1995d, ApJ, 449, 28
- Alcock, C. *et al.*, 1996a, ApJ, 461, 84 (A96)
- Alcock, C. *et al.*, 1996b, ApJ, submitted (astro-ph/9512146)
- Alcock, C. *et al.*, 1996c, ApJ, 463, L67
- Alcock, C. *et al.*, 1996d, ApJ, 471, in press (astro-ph/9604176)
- Alcock, C. *et al.*, 1996e, in preparation
- Alcock, C. *et al.*, 1996f, in preparation
- Alcock, C. *et al.*, 1996g, in preparation
- Ansari, R. *et al.*, 1995, A&A, 299, L21
- Aubourg, E. *et al.*, 1993, Nature, 365, 623
- Aubourg, E. *et al.*, 1995, A&A, 301, 1
- Aubourg, E. *et al.*, 1996, A&A, in press.
- Bahcall, J.N., Flynn, C., Gould, A. & Kirhakos, S., 1994, ApJ, 435, L51
- Bennett, D.P. *et al.*, 1995a, in "Dark Matter", AIP Conference Proceedings 316, 77.
- Bennett, D.P. *et al.*, 1995b, In *Clusters, Lensing, and the Future of the Universe*, ASP Conf. Series, 88, 95. (astro-ph/9510104)
- Bennett, D.P. *et al.*, 1996, to appear in Nucl. Phys. B (Supp.) (astro-ph/9606012).
- Bennett, D.P., & Rhie, S.H., 1996, preprint astro-ph/9603158.
- Burles, S. & Tytler, D. 1996, preprint astro-ph/9603070.
- Carr, B., 1994, ARA&A, 32, 531
- Carswell, R.F. *et al.* 1994, MNRAS, 268, L1.
- Charlot, S. & Silk, J., 1995, ApJ, 445, 124
- Della Valle, M., 1994, A&A, 287, L31
- De Rujula, A., Giudice, G.F., Mollerach, S., & Roulet, E., 1995, MNRAS, 275, 545
- Evans, N.W., 1993, MNRAS, 260, 191
- Fields, B.D., Mathews, G., & Schramm, D.N., 1996, astro-ph/9604095
- Flynn, C., Gould, A. & Bahcall, J.N., 1996, astro-ph/9603035
- Giraud, E., 1994, IAU Circ., 6097 and 6098
- Gould, A., 1994b, ApJ, 421, L75
- Gould, A., 1995b, ApJ, 441, 77
- Gould, A., 1995b, ApJ, 441, L21
- Gould, A. & Loeb, A., 1992, ApJ, 396, 104
- Gould, A., Miralda-Escude, J., & Bahcall, J.N., 1994, ApJ, 423, L105
- Griest, K., 1991, ApJ, 366, 412
- Hart, J. *et al.*, 1996, PASP, 108, 220
- Hu, E.M., Huang, J.S., Gilmore, G. & Cowie, L.L., 1994, Nature, 371, 493
- Kendall, M., & Stuart, A., 1979 "The Advanced Theory of Statistics", Macmillan, 1979
- Liebert, J., Dahn, C.C. & Monet, D.G., 1988, ApJ, 332, 891
- Mao, S. and Paczyński, B., 1991, ApJ, 374, L37
- Marshall, S.L. *et al.*, 1994, In *Astronomy From Wide Field Imaging*, IAU Symp. 161, ed. MacGillivray, H.T. *et al.*, Kluwer.
- Mushotzky, R., 1996, private communication.
- Paczynski, B, 1986, ApJ, 304, 1
- Paczynski, B, 1991, ApJ, 371, L63

- Paczynski, B, 1996, ARA&A, in press
- Pratt, M.R. *et al.*, 1995, In *Astrophysical Applications of Gravitational Lensing*, IAU Symp. 173, eds. Kochanek, C.S. & Hewitt, J.N, Kluwer. (astro-ph/9508039)
- Refsdal, S., 1964, MNRAS, 128, 295
- Roulet, E., Mollerach, S., 1996, *Phys. Rep.*, in press, (astro-ph/9603119)
- Rugers, M. & Hogan, C.J. 1996, preprint astro-ph/9603084.
- Sahu, K.C., 1994, Nature, 370, 275
- Songaila, A. *et al.* 1994, Nature, 368, 599.
- Stubbs, C.W. *et al.*, 1993, In *Charge Coupled Devices and Solid State Optical Sensors III*, ed. Blouke, M, *Proceedings of the SPIE*, 1900.
- Szymanski, M. *et al.*, 1994, *Acta Astronomica*, 44, 387
- Tytler, D., 1995, "Exploration of Neighboring Planetary Systems (ExNPS): Ground Based Element;" WWW address: <http://techinfo.jpl.nasa.gov/WWW/ExNPS/RoadMap.html>.
- Tytler, D, Fan, X.M., & Burles, S. 1996, preprint astro-ph/9603069.
- Udalski, A., Szymanski, M., Kaluzny, J., Kubiak, M., Krzeminski, W., Mateo, M., Preston, G.W., and Paczynski, B., 1994a, *Acta Astronomica*, 44, 165
- Udalski, A., Szymanski, M., Mao, S., Di Stefano, R., Kaluzny, J., Kubiak, M., Mateo, M. & Krzeminski, W., 1994b, ApJ, 436, L103
- White, S.D.M., Navarro, J.F., Evrard, A.E. & Frenk, C.S., 1993, Nature, 366, 429
- Wu, X-P., 1994. ApJ, 435, 66.
- Xu, J., Crotts, A.P.S., & Kunkel, W.E. 1995, ApJ, 451, 806.

TABLE 1  
FIELD CENTERS <sup>a</sup>

Field No.	Center: RA	Dec (2000)	Observations
1	05 05 21.3	-69 05 13	650
2	05 12 58.2	-68 28 16	456
3	05 22 36.3	-68 26 00	416
5	05 11 13.0	-69 41 00	501
6	05 19 54.4	-70 18 49	509
7	05 28 47.4	-70 29 46	618
9	05 11 07.4	-70 23 42	446
10	05 04 20.8	-69 53 56	363
11	05 37 07.6	-70 32 34	567
12	05 45 42.6	-70 34 44	435
13	05 19 41.7	-70 52 38	383
14	05 35 58.1	-71 09 20	379
15	05 45 46.4	-71 15 31	398
18	04 57 49.1	-68 55 46	313
19	05 06 10.3	-68 18 45	378
47	04 52 56.6	-68 00 27	300
77	05 27 27.1	-69 45 41	785
78	05 19 17.6	-69 43 39	745
79	05 12 53.1	-69 05 15	684
80	05 22 55.0	-69 04 00	634
81	05 36 19.0	-69 48 00	441
82	05 33 06.0	-69 03 00	426

<sup>a</sup> This table lists the 22 well-sampled fields used in the current analysis. We observe 82 LMC fields in total, but the remaining 60 were observed much less often ( $\sim 60$  observations each) in the first 2 years.

TABLE 2  
SELECTION CRITERIA

Description	Old	New	Change
Crowding	$f_{CRD} < 1.67$	$f_{CRD} < (\Delta\chi^2/(\chi^2/N_{\text{dof}}))^{10/9}/520$	Loosened
SN echo	$10' \times 10'$ square excl.	$10' \times 10'$ square excl.	Unchanged
Coverage	$\geq 3$ pts. on rise & fall	$\geq 1$ pt. on rise & fall	Loosened
High points	8 points $> 1\sigma$ high	6 points $> 1\sigma$ high	Loosened
Baseline fit	$\chi_{ml}^2/N_{\text{dof}} < 3$	$\chi_{ml-out}^2/N_{\text{dof}} < 4$	Loosened
Peak fit	$\chi_{peak}^2/N_{\text{dof}} < 4$	$\Delta\chi^2/(\chi_{peak}^2/N_{\text{dof}}) > 200$	Loosened
Chromaticity	$P_{\text{achrom}} < 0.997$	None	Loosened
Peak significance	$\Delta\chi^2/(\chi_{ml}^2/N_{\text{dof}}) > 200$	$\Delta\chi^2/(\chi_{ml}^2/N_{\text{dof}}) > 500$	Tightened
Amplification	$A_{\text{max}} > \max(1.50, 1 + 2\bar{\sigma})$	$A_{\text{max}} > \max(1.75, 1 + 2\bar{\sigma})$	Tightened

TABLE 3  
CANDIDATE MICROLENSING EVENTS

Event <sup>a</sup>	RA	Dec (2000)	V	V-R	$t_{\max}$	$\hat{t}$	$A_{\max}$	$f_{0R}$	$f_{0B}$	$\chi^2/N_{\text{dof}}$
1a	05 14 44.3	-68 48 01	19.6	0.6	57.08(3)	34.7(3)	7.2(1)	93.4(3)	63.0(3)	1.420
1b	05 14 44.3	-68 48 01	19.6	0.6	57.26(4)	34.3(3)	7.5(3)	77.7(2)	47.8(2)	1.134
4	05 17 14.6	-70 46 59	20.0	0.2	647.2(2)	46(2)	3.00(4)	35.6(2)	40.6(3)	1.416
5	05 16 41.1	-70 29 18	20.7	0.4	24.0(3)	82(2)	58(5)	26.5(4)	20.5(3)	1.680
6	05 26 14.0	-70 21 15	19.6	0.3	197.5(7)	87(4)	2.14(4)	57.1(5)	59.3(5)	0.873
7	05 04 03.4	-69 33 19	20.7	0.4	463.0(3)	115(3)	6.16(10)	23.2(3)	23.3(3)	1.447
8	05 25 09.4	-69 47 54	20.1	0.3	388.4(5)	62(2)	2.24(5)	35.1(4)	39.4(3)	2.218
9 <sup>b</sup>	05 20 20.3	-69 15 12	19.3	0.3	597.1(8)	147(3)	1.86(15)	77.5(4)	81.0(3)	6.868
10	05 01 16.0	-69 07 33	19.4	0.2	205.3(3)	42(1)	2.36(5)	67.4(3)	79.8(3)	1.982
11	05 34 21.8	-70 41 07	21.5	0.4	-8.6(3)	266(9)	11.9(4)	74(2)	64(2)	2.964
12a	05 33 51.7	-70 50 59	21.2	0.3	-10.0(3)	138(5)	7.2(4)	14.3(3)	14.6(3)	1.487
12b	05 33 51.7	-70 50 59	21.2	0.3	-11.4(8)	162(8)	6.8(2)	12.6(3)	11.5(2)	1.536

<sup>a</sup>Events 1-3 appeared in A96, but 2 & 3 are not in the sample used here. We number the current sample 1, 4 ... 12 to avoid ambiguity.

<sup>b</sup>Event 9 is the binary microlensing event; the parameters here are those resulting from a single-lens fit, and are not strictly appropriate.

The magnitudes and colors are based on an approximate transformation from our non-standard passbands. Time of peak magnification  $t_{\max}$  is in JD - 2,449,000. The microlensing fit parameters  $t_{\max}, \hat{t}, A_{\max}$  are defined in eq. 2. Units of  $f_{0B}, f_{0R}$  are arbitrary but are given for comparison with Table 4. The figure in brackets gives the formal  $1\sigma$  uncertainty of the least significant digit(s).

TABLE 4  
MICROLENSING FITS WITH BLENDING

Event	$t_{\max}$	$\hat{t}$	$A_{\max}$	$f_{lR}$	$f_{lB}$	$f_{uR}$	$f_{uB}$	$\chi^2/N_{\text{dof}}$
1a	57.08(3)	34.9(4)	7.25(16)	93(2)	62.0(9)	0(2)	1.2(1.0)	1.422
1b	57.26(4)	34.3(8)	7.5(3)	78(3)	48(2)	0(3)	0(2)	1.136
4	646.8(2)	79(13)	6.4(1.2)	14(4)	15(4)	21(4)	26(4)	1.383
5	24.0(3)	111(3)	220(70)	15.4(5)	15.6(4)	17.4(7)	0.0(2)	0.965
6	197.5(7)	94(3)	2.37(9)	47(3)	51(2)	10(3)	8(2)	0.875
7	463.0(3)	128(3)	7.1(2)	18.1(5)	21.7(3)	6.6(7)	0.0(2)	1.318
8	388.4(5)	62(3)	2.28(11)	35(3)	38(2)	0(3)	2(2)	2.227
9 <sup>a</sup>	603.04(2)	143.4(2)	()	20.57(13)	14.48(8)	58.8(3)	68.82(15)	1.755
10	205.3(3)	42.7(1.3)	2.40(5)	66(2)	78(3)	2(2)	2(3)	1.989

<sup>a</sup>For the binary microlensing event (9) the fit parameters given are for the binary lens fit described in (Bennett *et al.* 1996; Alcock *et al.* 1996e) Not all of the these parameters are appropriate for this fit.

Time of peak magnification  $t_{\max}$  is in JD - 2,449,000. The microlensing fit parameters  $t_{\max}$ ,  $\hat{t}$ , and  $A_{\max}$  are defined in eq. 2. The figure in brackets gives the formal  $1\sigma$  uncertainty of the least significant digit(s).



TABLE 5  
IMPACT PARAMETER DISTRIBUTION

Event Subset	$\langle u_{\min} \rangle$	$P(< u_{\min})$ <sup>a</sup>
1,5	0.080	0.032
1,5,7	0.109	0.024
1,4,5,7	0.169	0.061
1,4-7	0.237	0.194
1,4-8	0.279	0.343
1,4-8,10	0.304	0.466
1,4,5	0.170	0.097

<sup>a</sup>This is the probability that, given a number of detected events equal to that in the subsample, the mean  $u_{\min}$  would be smaller than the observed value in the previous column.

TABLE 6  
 SPATIAL DISTRIBUTION STATISTICAL TESTS

Events	bar bias	KS distance	$P_{KS}$	$P_{KS}$ (1-sided)	$P_{Wilcoxon}$
8	1	-0.268	0.546	0.273	0.83
8	4	+0.233	0.717	0.358	0.35
8	12	+0.386	0.140	0.070	0.12
6	1	-0.258	0.754	0.388	0.68
6	4	+0.318	0.495	0.243	0.28
6	12	+0.417	0.176	0.088	0.12

The results of the Kolmogorov-Smirnov 2-sided and 1-sided tests, and that of the Wilcoxon test on the distribution of distances from the lensing event locations to the center of the LMC bar for our 8 and 6 event samples are shown for models with ‘bar biases’ of 1 (halo lensing), 4, and 12. The ‘bar bias’ refers to the factor by which the microlensing optical depth in the bar exceeds the optical depth outside the bar. The sign on the KS distance is positive if the observed distribution is more uniform than the model. The 1-sided KS probabilities refer to 1-sided KS tests of bias = 1 models against the bias > 1 hypothesis and the bias = 4 or 12 models against the bias < 4 or bias < 12 hypotheses. The Wilcoxon probability is that the bar distances from the observations are *not* systematically greater than those predicted by the models.

TABLE 7  
SINGLE EVENT OPTICAL DEPTHS

Event	$\hat{t}$	$\hat{t}_{bl}$	$\tau_1$
1	34.7	38.8	$1.8 \times 10^{-8}$
4	46	52	$2.3 \times 10^{-8}$
5	82	88	$3.5 \times 10^{-8}$
6	87	100	$4.1 \times 10^{-8}$
7	115	131	$6.0 \times 10^{-8}$
8	62	70	$2.8 \times 10^{-8}$
9	147	143	$6.6 \times 10^{-8}$
10	42	47	$2.1 \times 10^{-8}$

The quantity  $\hat{t}_{bl}$  is the average actual event timescale for events in our Monte Carlo calculations which are detected with an unblended fit timescale of  $\hat{t}$ .  $\hat{t}_{bl}$  can be used as an unbiased estimator of the actual  $\hat{t}$  value. For the binary event, # 9, the blended fit  $\hat{t}$  value is used instead.  $\tau_1$  indicates the contribution of each event to the total microlensing optical depth, computed using equation (6).

TABLE 8  
OPTICAL DEPTH CONFIDENCE INTERVALS

$\mathcal{E}$ type	# of events	$\tau(10^{-7})$ for confidence level:						
		0.025	0.05	0.16	measured	0.84	0.95	0.975
<b>photometric</b>	<b>8</b>	<b>1.24</b>	<b>1.47</b>	<b>1.99</b>	<b>2.93</b>	<b>4.30</b>	<b>5.28</b>	<b>5.82</b>
sampling	8	1.12	1.31	1.77	2.59	3.79	4.66	5.12
photometric $\hat{t}$ -fit	8	1.33	1.55	2.10	3.06	4.49	5.53	6.07
sampling $\hat{t}$ -fit	8	1.18	1.38	1.85	2.71	3.95	4.85	5.32
sampling no $\hat{t}$ -cor.	8	1.00	1.17	1.60	2.34	3.44	4.23	4.67
photometric	6	0.77	0.93	1.33	2.06	3.18	4.00	4.44
sampling no $\hat{t}$ -cor.	6	0.61	0.74	1.04	1.59	2.43	3.06	3.40

The table entries show limits at various confidence levels on the microlensing optical depth  $\tau$  in units of  $10^{-7}$ , with different assumptions for the detection efficiency  $\mathcal{E}$ , different  $\hat{t}$  corrections (due to blending), and 6 or 8 events assumed to be microlensing. Our photometric efficiencies are considered the most accurate estimate of the true microlensing detection efficiency, and the average  $\hat{t}$  correction is preferred because it is unbiased. The photometric efficiency results with the average  $\hat{t}$  correction are displayed in bold face type. The ‘no  $\hat{t}$  correction’ values are to be considered extreme lower limit values.

TABLE 9  
MAXIMUM LIKELIHOOD FITS

Events <sup>a</sup>	Model <sup>b</sup>	Halo	$m_{ML}(\text{M}_{\odot})$ <sup>c</sup>	$f_{ML}$	$f_{ML}M_H(10^{10}\text{M}_{\odot})$	$\tau_{ML}(10^{-8})$
6	S	med.	$0.46^{+0.30}_{-0.17}$	$0.50^{+0.30}_{-0.20}$	$20^{+12}_{-7}$	$24^{+14}_{-8}$
6	A	med.	$0.32^{+0.25}_{-0.11}$	$0.41^{+0.25}_{-0.17}$	$19^{+11}_{-8}$	$23^{+14}_{-9}$
6	B	large	$0.55^{+0.38}_{-0.21}$	$0.30^{+0.19}_{-0.12}$	$22^{+14}_{-9}$	$24^{+15}_{-10}$
6	C	small	$0.21^{+0.12}_{-0.08}$	$0.61^{+0.36}_{-0.25}$	$14^{+8}_{-6}$	$18^{+11}_{-8}$
6	D	E6	$0.31^{+0.18}_{-0.11}$	$0.37^{+0.22}_{-0.15}$	$17^{+10}_{-7}$	$22^{+13}_{-8}$
6	E	max disk	$0.04^{+0.02}_{-0.01}$	$2.8^{+?}_{-?}$	$22^{+?}_{-?}$	$24^{+?}_{-?}$
6	F	big disk	$0.13^{+0.08}_{-0.05}$	$1.2^{+0.70}_{-0.47}$	$25^{+14}_{-10}$	$23^{+13}_{-9}$
6	G	big disk	$0.21^{+0.12}_{-0.08}$	$0.71^{+0.44}_{-0.29}$	$23^{+14}_{-9}$	$23^{+14}_{-10}$
8	S	med.	$0.45^{+0.24}_{-0.15}$	$0.68^{+0.33}_{-0.23}$	$28^{+13}_{-9}$	$32^{+16}_{-11}$
8	A	med.	$0.32^{+0.20}_{-0.09}$	$0.55^{+0.28}_{-0.20}$	$25^{+13}_{-9}$	$31^{+16}_{-11}$
8	B	large	$0.56^{+0.31}_{-0.20}$	$0.41^{+0.21}_{-0.15}$	$29^{+15}_{-11}$	$33^{+17}_{-12}$
8	C	small	$0.21^{+0.11}_{-0.07}$	$0.83^{+0.40}_{-0.29}$	$19^{+9}_{-7}$	$25^{+12}_{-9}$
8	D	E6	$0.31^{+0.16}_{-0.11}$	$0.50^{+0.25}_{-0.18}$	$23^{+12}_{-8}$	$30^{+15}_{-11}$
8	E	max disk	$0.04^{+0.02}_{-0.01}$	$> 1$	?	?
8	F	big disk	$0.13^{+0.06}_{-0.04}$	$1.67^{+0.70}_{-0.52}$	$34^{+14}_{-11}$	$32^{+14}_{-10}$
8	G	big disk	$0.20^{+0.11}_{-0.07}$	$0.97^{+0.49}_{-0.34}$	$31^{+16}_{-11}$	$32^{+16}_{-11}$

<sup>a</sup> This column shows the number of events assumed to result from halo microlensing. The 8-event sample is 1,4...10 ; the 6-event sample excludes events 9 & 10.

<sup>b</sup>The models are defined as in A96; in summary, model S is given by eq. 8, the others are Evans models. Model A is similar to model S. Models B and C have more and less massive halos; model D is similar to A but flattened to E6. Model E is an extreme maximal disk/minimal halo model, while F and G are more realistic heavy disk/ light halo models.

<sup>c</sup>Columns 4 & 5 show the maximum likelihood Macho mass and halo fraction from Section 6.6. Columns 6 & 7 show the implied total mass of Machos within 50 kpc of the Galactic center, and the resulting optical depth. For model (E) some entries are marked “?” indicating that the halo fraction became unreasonably large and the numerically calculated error estimates were therefore inaccurate.

TABLE 10  
MICROLENSING BY STARS <sup>a</sup>

Population	$\tau(10^{-7})$	$\langle \hat{t} \rangle$ (days)	$\langle l \rangle$ (kpc)	$\Gamma(10^{-7}\text{yr}^{-1})$	$N_{\text{exp}}$
Thin disk	0.15	112	0.96	0.62	0.29
Thick disk	0.036	105	3.0	0.16	0.075
Spheroid	0.029	95	8.2	0.14	0.066
LMC center	0.53	93	49.8	2.66	(1.19)
LMC average	0.32	93	49.8	1.60	0.71
Halo S	4.7	89	14.4	24.3	11.2

<sup>a</sup>This table shows microlensing quantities for model stellar populations, with Scalo PDMF and the density and velocity distributions given in A96.  $\langle l \rangle$  is the mean lens distance.  $\Gamma$  is the total theoretical microlensing rate. The expected number of events  $N_{\text{exp}}$  includes our detection efficiency averaged over the  $\hat{t}$  distribution. For the LMC, two rows are shown; firstly at the center, and secondly averaged over the location of our fields; only the averaged  $N_{\text{exp}}$  is relevant.